

HST/ACS Photometry of Old Stars in NGC 1569: The Star Formation History of a Nearby Starburst¹

Aaron J. Grocholski^{2,3,4}, Roeland P. van der Marel², Alessandra Aloisi², Francesca Annibali⁵, Laura Greggio⁶, Monica Tosi⁵

ABSTRACT

We used HST/ACS to obtain deep V - and I -band images of NGC 1569, one of the closest and strongest starburst galaxies in the Universe. These data allowed us to study the underlying *old* stellar population, aimed at understanding NGC 1569's evolution over a full Hubble time. We focus on the less-crowded outer region of the galaxy, for which the color-magnitude diagram (CMD) shows predominantly a red giant branch (RGB) that reaches down to the red clump/horizontal branch feature (RC/HB). A simple stellar population (SSP) analysis gives clear evidence for a more complicated star formation history (SFH) in the outer region. We derive the full SFH using a newly developed code, SFHMATRIX, which fits the CMD Hess diagram by solving a non-negative least squares problem. Our analysis shows that the relative brightnesses of the RGB tip and RC/HB, along with the curvature and color of the RGB, provide enough information to ameliorate the age-metallicity-extinction degeneracy. The distance/reddening combination that best fits the data is $E(B - V) = 0.58 \pm 0.03$ and $D = 3.06 \pm 0.18$ Mpc. Star formation began ~ 13 Gyr ago, and this accounts for the majority of the mass in the outer region. However, the initial burst was followed by a relatively low, but constant, rate of star formation until ~ 0.5 - 0.7 Gyr ago

¹Based on observations with the NASA/ESA *Hubble Space Telescope*, obtained at the Space Telescope Science Institute, which is operated by AURA for NASA under contract NAS 5-26555

²Space Telescope Science Institute, 3700 San Martin Dr., Baltimore, MD 21218, USA; aloisi, marel@stsci.edu

³Astronomy Department, Yale University, New Haven, CT, 06520, USA

⁴current address: Department of Astronomy, University of Florida, Gainesville, FL 32607, USA; a.grocholski@astro.ufl.edu

⁵Osservatorio Astronomico di Bologna, INAF, Via Ranzani 1, I-40127 Bologna, Italy; francesca.annibali, monica.tosi@oabo.inaf.it

⁶Osservatorio Astronomico di Padova, INAF, vicolo dell'Osservatorio 5, 35122 Padova, Italy; laura.greggio@oapd.inaf.it

when there may have been a short, low intensity burst of star formation. Stellar metallicity increases over time, consistent with chemical evolution expectations. The dominant old population shows a considerable spread in metallicity, similar to the Milky Way halo. However, the star formation in NGC 1569’s outer region lasted much longer than in the Milky Way. The distance and line-of-sight velocity of NGC 1569 indicate that it has moved through the IC 342 group of galaxies, which may have caused this extended star formation. Comparison with other recent work provides no evidence for radial population gradients in the old population of NGC 1569, suggesting that our results are representative of the old stellar population throughout the galaxy.

Subject headings: galaxies: dwarf — galaxies: evolution — galaxies: individual (NGC 1569) — galaxies: irregular — galaxies: stellar content

1. Introduction

At high redshift, the star formation rate density is considerably higher than what we observe in the local Universe (e.g., Hopkins & Beacom 2006). Many galaxies, such as Lyman break galaxies, are thought to be undergoing massive bursts of star formation. These starbursts are important to understand since they drive the evolution of galaxies. Energy generated in a starburst provides thermal and mechanical heating to the host galaxy, and supernova winds spread chemically enriched material throughout the ISM. In some cases, starbursts have enough energy to create a galactic wind that escapes the gravitational potential of the host galaxy and thereby disperses metals throughout the intergalactic medium (e.g., Veilleux et al. 2005).

Given the unresolved nature of high redshift galaxies, the information we can glean from them has its limits. One approach to understand the physical processes at work during the starburst phase of high redshift galaxies is to turn to studies of nearby starburst galaxies (although these may represent quite a different mass and evolutionary stage). Although they are rare, the proximity of starburst galaxies in the local Universe allows us to resolve them into individual stars and thereby study their star formation histories (SFHs) in great detail over the lifetime of the galaxy.

A starburst is loosely defined as an intense period of star formation that is unsustainable over a Hubble time due to the limited supply of gas available in the galaxy. Starbursts in the local Universe are typically found in dwarf irregular (dIrr) and blue compact dwarf (BCD) galaxies, systems which are characterized by their relatively blue colors due to young stellar

populations, high gas content, and low metallicities. In some cases, their metal abundances are so low that these galaxies have been targeted as possible primeval galaxies that may have only recently begun forming stars (Izotov & Thuan 1999). However, in all dIrrs and BCDs that have been observed to a sufficient photometric depth, red giant branch stars (RGB; i.e., evolved stars older than ~ 1 Gyr) have been detected, proving that these galaxies have been forming stars for an extended period of time (e.g., I Zw 18, Aloisi et al. 2007; SBS 1415+437, Aloisi et al. 2005; I Zw 36, Schulte-Ladbeck et al. 2001).

The dIrr galaxy NGC 1569 is one of the closest and most extreme starbursts. NGC 1569 has a total dynamical mass of $M = 3.3 \times 10^8 M_{\odot}$, 1/3 of which is in HI (Israel 1988). With a mean oxygen abundance of $12 + \log(O/H) = 8.2 \pm 0.2$ (or $Z = 0.25Z_{\odot}$, assuming $[O/Fe] = 0.0$; Greggio et al. 1998 and references therein), NGC 1569 is thus a gas-rich system with an SMC-like chemical composition. Long assumed to lie at a distance of 2.2 Mpc (Israel 1988), in Grocholski et al. (2008) we unequivocally identified for the first time the tip of the red giant branch (TRGB) and found that its true distance is ~ 3 Mpc (see also §5.1). This makes it a likely member of the IC 342 group of galaxies. In the past ~ 25 Myr, NGC 1569 has formed a large number (~ 150) of star clusters with masses similar to Milky Way open clusters (Anders et al. 2004; see also Origlia et al. 2001, Hunter et al. 2000), as well as three super star clusters. Based on our improved distance, the three super star clusters, NGC 1569-A1 and NGC 1569-A2 (de Marchi et al. 1997, Gilbert & Graham 2002) and NGC 1569-B (Larsen et al. 2008) have masses of $(6-7) \times 10^5 M_{\odot}$. These clusters, which are more massive than any of the young clusters in the Milky Way or Large Magellanic Cloud, will likely survive for the entire lifetime of the galaxy, thus making them possible precursors to globular clusters. Many authors have studied the recent star formation in NGC 1569 using various tracers of the ISM, including: CO (Young et al. 1984; Greve et al. 1996; Taylor et al. 1999); HI (Israel & van Driel 1990; Stil & Israel 1998); $H\alpha$ (Hunter et al. 1993; Devost et al. 1997); and the X-ray emission from hot gas (Heckman et al. 1995; della Ceca et al. 1996; Martin et al. 2002). All of these indicators point towards an ISM heavily impacted by a starburst driven galactic superwind.

Star formation in the central region of NGC 1569 has been studied by a number of authors using HST photometry (e.g., Vallenari & Bomans 1996; Greggio et al. 1998; Angeretti et al. 2005). The most straightforward way to determine a galaxy’s SFH is by comparing its observed color-magnitude diagram (CMD) to synthetic CMDs, created from stellar evolution models, with star formation rates that vary over time. Both Greggio et al. (1998) and Angeretti et al. (2005) used this method to determine the SFH of NGC 1569 and found that in the past ~ 1 Gyr, NGC 1569’s star formation rate per unit area is 2-3 times higher than in other strong starbursts and 2-3 orders of magnitude higher than what is seen in Local Group irregulars and the solar neighborhood. At such a rate, the star formation in NGC

1569 would have exhausted its gas supply in ~ 1 Gyr. Thus, to have sustained star formation for an extended period of time, NGC 1569 would need to have accreted gas, possibly from a nearby HI cloud (Mühle et al. 2005; Stil & Israel 1998). However, since neither program’s data reached the faint magnitudes needed to sample the RGB, they were not able to constrain NGC 1569’s SFH prior to 1 Gyr ago.

While the existence of an RGB indicates stars older than 1 Gyr, the age-metallicity degeneracy of these stars makes it difficult to resolve the age distribution of stars from the RGB alone. The most accurate way to determine the SFH of any stellar population is by resolving the main sequence turn off (MSTO) for even the oldest stars. However, at $M_I \sim 4$ for 13 Gyr old stars, the MSTO is too faint to be observed in a reasonable amount of telescope time for galaxies outside of about 1 Mpc. So instead, we must turn to brighter CMD features, such as the core helium burning stars of the red clump/horizontal branch (RC/HB; $M_I \sim -0.2$) to help lift the age-metallicity degeneracy. Rejkuba et al. (2005) and Rejkuba et al. (2011) analyzed a CMD of the elliptical galaxy Cen A (NGC 5128) that reached 0.5 mag below the RC/HB and showed that photometry reaching these depths can provide enough information to determine a galaxy’s SFH over a Hubble time. Therefore, to determine the SFH of NGC 1569’s oldest stars, we obtained deep HST ACS/WFC V - and I -band images that reach down to the RC/HB and cover both the crowded inner and relatively sparsely populated outer regions (HST GO-10885, PI: A. Aloisi). Our observational program was designed to reach ~ 0.5 mag below the RC/HB. However, since NGC 1569 is roughly 50% farther away than previously believed, our photometry only barely reaches the RC/HB and not well below it. Recently, as a part of a study of 18 nearby dwarf starburst galaxies, McQuinn et al. (2010) analyzed a subset of our images. Using the CMD fitting program, MATCH (Dolphin 2002), they determined the full SFH of NGC 1569. Although they focused primarily on the starburst properties, they also determine a relatively coarse age distribution for stars older than 1 Gyr. We will discuss their results further in §5.3.

Since the SFH of young stars in NGC 1569 has been well studied by previous authors, in this paper we present an analysis focused on the SFH of stars older than 1 Gyr. In Grocholski et al. (2008) we showed that the recent star formation is concentrated in the core of NGC 1569, while the outer region shows no signs of a significant young population. In Grocholski et al. (2008) we adopted the convention of referring to the bottom half of our NGC 1569 field (Fig. 1) as the core and the top half as the halo. Recently, in Ryś et al. (2011), we used four WFPC2 fields to study the number density profile of RGB stars in NGC 1569 out to 8 scale radii and found that NGC 1569 does appear to transition from an exponential disk to a halo population. However, as this occurs outside of our ACS field, herein we refer to the upper half of our ACS field as the outer region of NGC 1569. Due to the fact that the outer region is much less crowded than the core, these data necessarily

go deeper, allowing us to more accurately detect and measure the brightness of stars on the RC/HB. This is illustrated by the luminosity functions (LFs) in Fig. 4 of Grocholski et al. (2008), where the peak due to the RC/HB is visible in the outer region, but not in the core. Therefore, herein we focus solely on our observations of NGC 1569’s outer region.

In §2 we present our data and detail the process used to determine the photometry and errors. The resulting CMDs for the core and outer region are discussed in §3. In §4 we test whether or not NGC 1569’s outer region can be treated as a simple stellar population (i.e., if it can be represented by a single age, single metallicity population) while in §5 we use the method of synthetic CMD fitting to determine the full SFH of NGC 1569 and compare our results to the work of McQuinn et al. (2010). In §6 we discuss NGC 1569’s SFH in the context of interactions with the IC 342 group of galaxies. Conclusions are summarized in §7. Appendix A provides an overview of our new code SFHMATRIX for determining the SFH a galaxy.

2. Imaging Data

2.1. HST/ACS Observations

We observed NGC 1569 with the HST ACS/WFC in November 2006 and January 2007 as a part of HST program GO-10885 (PI: Aloisi). Images were taken in the F606W (V) and F814W (I) broad-band filters as well as the F658N ($H\alpha$) narrow-band filter. Total exposure times were: 61716 s in the V -band, composed of 54 individual images; 24088 s in the I -band, composed of 22 images, and 4620 s in the $H\alpha$ filter, composed of 4 images. While all of the images were centered on the galaxy, telescope rotation between the two observation dates caused both the V - and I -band images to be split between two different orientation angles. NGC 1569 was only imaged in $H\alpha$ during the second visit and, therefore, these data are only at one orientation. WFPC2 was used in parallel to image regions in the outskirts of NGC 1569, $\sim 6'$ from the galaxy’s center, also in the V - and I -bands. These data are discussed in Ryś et al. (2011).

Our ACS images were dithered using a standard sub-pixel plus integer dither pattern. The sub-pixel pattern is used to improve the sampling of the point spread function (PSF) and aid in the removal of bad/hot pixels and cosmic rays. The integer pixel step is necessary to fill in the gap between the ACS chips. While these are the same data that were presented in Grocholski et al. (2008), we have reprocessed all of the images using the most up-to-date versions of the ACS pipeline (CALACS) and calibration frames. Images in each filter were then combined into a single image using the MULTIDRIZZLE software package (Fruchter et al.

2009). The MULTIDRIZZLE software fine-tunes the image alignment, corrects for small shifts, rotations, and geometric distortions between the images, and removes cosmic rays and bad pixels. We experimented with the drizzle parameters within MULTIDRIZZLE and found that resampling the images to 0.7 times the original ACS/WFC pixel scale provides the best resolution and PSF sampling for our data. Our final combined images have a pixel size of $0.035''$ and cover roughly $3.5' \times 3.5'$. Figure 1 shows our 3-color image of NGC 1569. The $H\alpha$ image was not used for photometry and is thus excluded from further discussion in this paper.

2.2. Photometry and Calibration

Using the stand-alone versions of DAOPHOT and ALLSTAR (Stetson 1987), we performed photometry on the V - and I -band images in the following manner. We created a rough PSF model from ~ 300 bright, uncrowded stars in each image. This rough model was then used to remove neighbors from around the full set of ~ 1000 PSF stars in each image, thereby allowing us to create a more robust PSF. Our PSF stars were chosen to have excellent spatial coverage across the entire image so as to accurately model variations in the PSF shape as a function of position. We note that, due to crowding effects, we have avoided using any stars in the crowded inner region of NGC 1569. Next, we used ALLSTAR to fit the improved PSF model to independent source detection lists for the V - and I -band images. In an effort to find and measure faint stars, we performed a single iteration of subtracting from the images all sources measured in the first ALLSTAR run, searching for previously undetected objects, adding those objects to the original source detection list, and then re-running the PSF fitting on the original images, this time using the newly updated catalog.

We matched the V and I photometry lists, requiring that detections were within 0.5 pixel to be considered a match. The resulting photometric catalog contains over 400,000 sources. To further clean our catalog of false detections or background galaxies, we made cuts by both position and photometric quality. Positional cuts were used to trim detections from around overexposed stars, where diffraction spikes can lead to false detections, as well as from the edges of the images and the ACS chip gap, which had lower exposure time due to dithering and therefore a much higher incidence of noise peaks that were coincident between the V and I images. ALLSTAR provides three estimates of the quality of the PSF fit to any given source: σ , the error in the PSF magnitude; χ , the goodness-of-fit for the PSF fit to each star; and *sharpness*, a measure of the intrinsic size of the source relative to the PSF. Assuming that noise peaks follow a Gaussian distribution around the mean background level, we expect on the order of one noise peak that meets our matching criteria

and lies 3.5σ above the mean in *both* bands. Since a signal-to-noise ratio of 3.5 translates to an error of ~ 0.3 mag, we keep only those stars with $\sigma_V \leq 0.3$ and $\sigma_I \leq 0.3$. Sources with a *sharpness* $\ll 0$ are considerably more narrow than the PSF and are likely to be false detections, while those with *sharpness* $\gg 0$ are more extended and likely to be background galaxies or stellar blends. Thus, we cut from our catalog any stars with $|sharpness| > 1$ in either band. We have chosen to not make any cuts based on χ since most of the faint objects with large χ values have already been cut based on their σ and *sharpness* values. Bright sources with large χ values are generally real stars, with the large χ due to inadequacies in the PSF (which appear more significant when the star is bright and the noise is low). After applying all of the above cuts, our photometric catalog contains over 370,000 stars, with approximately 31,000 of those stars residing in the outer region.

Finally, we apply the necessary zeropoints and corrections to place our photometry on the Johnson-Cousins magnitude system following the prescriptions in Sirianni et al. (2005). First, we converted instrumental magnitudes to the HST VEGAMAG system according to the equation

$$m_{vegagmag} = m_i + C_{ap} + ZP - C_{inf} + C_{sky} + C_{cte}. \quad (1)$$

m_i is the PSF-fitting magnitude $[-2.5 \times \log(flux)]$ within a radius of 10 pixels ($0.35''$) and C_{ap} is the correction necessary to convert that magnitude to the conventional $0.5''$ radius aperture. ZP is the HST VEGAMAG zeropoint¹ for a given filter and C_{inf} is an offset to convert magnitudes from the $0.5''$ radius aperture to an infinite aperture (Sirianni et al. 2005). C_{sky} corrects for the fact that our aperture correction, C_{ap} , uses an annulus that is a finite distance from the star to estimate the sky background. Since a small amount of star light is included in the annulus, the sky background is overestimated in the aperture correction step. The ACS CCDs suffer from losses in charge transfer efficiency (CTE) as a result of their prolonged exposure to radiation in space. We corrected for CTE losses following the prescription in Riess & Mack (2004), namely,

$$C_{cte} = 10^A \times SKY^B \times FLUX^C \times \frac{Y}{2048} \times \frac{MJD - 52333}{365}, \quad (2)$$

where SKY is the sky background counts per pixel, $FLUX$ is the star counts per exposure within our PSF fitting radius, Y is the number of charge transfers, and MJD is the Modified Julian Date. The coefficients were taken from Riess & Mack (2004) for an aperture radius of $r = 7$ pixels on the native pixel scale (or 10 pixels on our resampled drizzled image), and are $A = -0.7$, $B = -0.34$, and $C = -0.36$. Due to the fact that our images were both dithered and taken at two different orientations, each star has 54 different charge transfer values, Y ,

¹<http://www.stsci.edu/hst/acs/analysis/zeropoints>

in the V -band and 22 different Y values in the I -band. We tested two approaches for dealing with this in calculating C_{cte} for each star. First, we calculated the CTE corrections for each star in each individual image and averaged those together to get C_{cte} for each star. In the second approach, we determine the average number of charge transfers for each star and then calculate a single CTE correction for each star. We found that these two approaches give similar C_{cte} values for each star. Our average CTE correction is ~ 0.01 mag, but can be as large as ~ 0.2 mag for the faintest stars. After applying all of the zeropoints and corrections, the last step in our calibration was to convert photometry on the VEGAMAG system to the Johnson-Cousins system by following the procedure outlined in Sirianni et al. (2005). Note that we have not applied any reddening corrections to our photometry since these are included as part of our models (see §4 and §5).

2.3. Completeness and Errors

To properly evaluate the role of incompleteness and photometric errors in the analysis of our data, we performed artificial star tests on our V - and I -band images. We added artificial stars to our images using the ADDSTAR routine within DAOPHOT. This routine simulates real stars covering a user supplied range of positions and magnitudes by adding the appropriate Poisson noise to the previously generated PSFs. In an effort to compromise between efficient computing of the completeness and not changing the crowding on the images, we divided the images into a grid of boxes 30 pixels \times 30 pixels in size and placed one artificial star in each box, with the added restriction that no two artificial stars lie within two PSF fitting radii (20 pixels) of each other. To fully sample the images, we varied both the starting position of the grid as well as the position of the artificial star within each box, allowing for shifts as small as 0.01 pixels. We chose the range of magnitudes covered by the artificial stars to extend ~ 1 mag brighter and fainter than the observed data. To better mimic the observed luminosity function, we generated twice as many artificial stars in the faint half of the magnitude range as in the bright half. After placing the artificial stars on the image, we followed the same procedure as outlined in the previous section and performed PSF fitting on the entire image. We then cross-correlated the input artificial star list with the output photometric catalog, again using a 0.5 pixel matching radius. An artificial star was considered to be “lost” if it was not matched in the output catalog, or if its PSF fitting magnitude differs from its input magnitude by more than 0.75 mag, it has $\sigma > 0.3$ or $|sharpness| > 1$. We note that we also trimmed the artificial stars by position in the same way as for the observed catalog, but these stars were not counted in the lost/recovered statistics. In the outer region, we simulated over 170,000 stars in each band, or more than 5 times the number of stars observed in the outer region.

3. Color-Magnitude Diagrams

In Figs. 2 and 3 we present the resulting CMDs for the core and outer region of NGC 1569. Previous authors have shown that NGC 1569 has recently undergone massive bursts of star formation (e.g., Greggio et al. 1998; Angeretti et al. 2005). This is evident in the CMD of the core (Fig. 2), which is dominated by features that are due to young stellar populations. Readily visible above $I \sim 24$ and with $0.6 \lesssim (V - I) \lesssim 1.1$ is the blue plume, which contains both young ($\lesssim 10$ Myr) main sequence stars and massive evolved stars ($\gtrsim 9 M_{\odot}$) on the blue part of their core helium-burning phase. The red plume of supergiants at $1.9 \lesssim (V - I) \lesssim 2.5$ and the blue loop stars (between the red and blue plumes) indicate the existence of evolved stars with masses $\gtrsim 5 M_{\odot}$. Also visible at $I \sim 24$ and $(V - I) \gtrsim 2.5$ are the intermediate-mass ($\sim 1.2 - 6 M_{\odot}$) carbon stars of the thermally pulsating asymptotic giant branch (AGB), as well as M-type AGB stars.

Unlike the core, the CMD of the outer region (Fig. 3) shows no signs of a significant young stellar population, indicating that the recent bursts of star formation in NGC 1569 were restricted to the core. In the outer region, the only outstanding feature is the upper ~ 4 mag of the red giant branch (RGB), which is the result of stars older than ~ 1 Gyr that have evolved off of the main sequence and are expanding as their He cores increase in mass, contract, and work their way toward becoming fully degenerate. RGB stars are also present in the core, though heavily blended in the CMD with younger evolutionary features, indicating a global star formation history that began at least 1 Gyr ago.

Given NGC 1569’s location ($\ell = 143^{\circ}68213$, $b = 11^{\circ}24174$) near the Galactic Plane, we expect our CMDs to suffer from some foreground contamination due to the Galaxy. This contamination can be seen in Fig. 3 as the swath of stars stretching from $I \sim 19$, $(V - I) \sim 1$ to $I \sim 25$, $(V - I) \sim 4$. In Fig. 4, we confirm that this “feature” is due to the Milky Way by plotting a CMD of the expected foreground stars in our ACS field based on the Besançon model of the Galaxy (Robin et al. 2003). The Besançon model includes four populations: the thin disk, thick disk, bulge, and spheroid. The plume of faint stars around $V - I \sim 1.3$ is due to white dwarfs in the disk, and the stars in top right part of the CMD are primarily M-dwarfs in the disk. These foreground stars are not considered further in the remainder of this paper. We note that after taking into account the foreground stars, there is a sparse blue ($V - I \sim 0.4$ in Fig. 3) plume of stars in the outer region that are not related to the old RGB stars. These stars are spread throughout the outer region, but with a higher concentration toward the core of the galaxy, and are possibly young stars that have migrated out of the core (§5.3).

4. Luminosity Function Analysis with Simple Stellar Population Models

As we have shown above, the outer region of NGC 1569 appears to be a purely old population and thus provides the opportunity to study the SFH of stars older than ~ 1 Gyr. Since we have no *a priori* reason to assume a specific SFH for the outer region (e.g., that it formed in a single burst or experienced extended episodes of star formation), we begin with the most straightforward approach of treating NGC 1569’s outer region as a simple stellar population (SSP), i.e., one that can be fit by a theoretical isochrone with a single age and metallicity. Models with more complicated SFHs are addressed in §5. For both the SSP analysis and full SFH analysis, we use stellar evolution models from the Padova group² (e.g., Marigo et al. 2008) as they provide comprehensive coverage of the stages of stellar evolution and are readily available for a large range of ages, metallicities, and photometric systems.

The metallicity of an isochrone is Z . Throughout this paper we will often use instead the approximation $\log(Z/Z_{\odot}) = [\text{Fe}/\text{H}]$, where the equality holds for a solar composition mix. Like the Padova models, we adopt $Z_{\odot} = 0.019$ from work by Anders & Grevesse (1989)³

4.1. Theoretical RGB Luminosity Function

The RGB contains a plethora of information, with age, metallicity, distance, and reddening all playing a role in the luminosity, shape and color of the RGB. For a large range of ages and abundances, the I -band luminosity of the tip of the RGB (TRGB) is approximately constant at $M_I \sim -4.0$ (e.g., Barker et al. 2004), thus acting as a standard candle. Unfortunately, while the shape of the RGB can place some constraints on $[\text{Fe}/\text{H}]$, the RGB color suffers from a well known degeneracy, where different combinations of age, metallicity, and reddening can create RGBs that are similar in appearance.

Rather than dealing with the RGB as a whole, we instead turn to three features that may be visible in the LF of the RGB: the HB/RC, RGB bump, and AGB bump. The HB/RC feature on the CMD is a collection of evolved stars that are in their core helium burning phase. The exact luminosity of the RC/HB is dependent on both the age and metallicity of the stars (e.g., Grocholski & Sarajedini 2002, Girardi & Salaris 2001), but is roughly $3.5 - 4$

²<http://stev.oapd.inaf.it/cgi-bin/cmd>

³There are many indications for a lower value of $Z_{\odot} = 0.0134$ as advocated by Asplund et al. (2009), but it has so far not been possible to bring such a lower number in agreement with Solar sound speed measurements from helioseismology. Recent 3D modeling of the solar photosphere from Caffau et al. (2011) gives $Z_{\odot} = 0.0153$, which moves in the direction of reconciling solar photosphere and helioseismology measurements.

mag fainter than the TRGB in the I -band (Fig. 5).

Both the RGB bump and AGB bump are more subtle features that are typically not identifiable in the CMD of a stellar population and are only sometimes visible as discrete “bumps” in the LF. The RGB bump feature occurs when the H burning shell in RGB stars moves outward and crosses the chemical discontinuity produced during the first dredge up. Since the luminosity of the H burning shell, L_H , is related to the mean molecular weight, μ , as $L_H \propto \mu^7$, the sudden drop in μ at the discontinuity (due to an increase in the H abundance) causes a temporary drop in the luminosity of an RGB star. RGB stars spend $\sim 20\%$ of their total RGB lifetime in the bump phase. Due to the fact that the depth of the chemical discontinuity is dependent on both the mass and composition of the star, the luminosity of the RGB bump acts as a tracer of the age and metallicity (Fig. 6). Following central He exhaustion, RC/HB stars evolve up the AGB. The transition from core helium burning to a thick He shell burning configuration causes a temporary drop in the luminosity of AGB stars, which results in the formation of the AGB bump. Fig. 7 shows that the luminosity of the AGB bump is primarily dependent on the age of the population, with $[\text{Fe}/\text{H}]$ playing a role only for the most metal rich systems.

Based on theoretical models, the RC/HB is visible in all stellar populations with $\log(\text{age}) \gtrsim 8.8$ (630 Myr), regardless of $[\text{Fe}/\text{H}]$. On the other hand, while both the RGB bump and AGB bump features form in stellar populations with $\log(\text{age}) \gtrsim 9.1$ (1.25 Gyr), these features cannot always be identified in a LF. Aside from situations where the number of stars is so low that few stars exist on the RGB (e.g., open clusters), the significant range in brightness of the RGB bump (> 2.5 mag) can cause it to overlap with either the AGB bump or the RC/HB. In contrast, the AGB bump varies in brightness by less than 0.5 mag and is never less than 1.0 mag brighter than the RC/HB. This gives rise to stellar populations that can have either two or three distinct bumps in their LFs, assuming they are well populated. Although there is still some age/metallicity degeneracy with the RC/HB, RGB bump and AGB bump, by analyzing the brightness of each of these features relative to each other and relative to the TRGB, we can eliminate any dependence on distance and reddening and place considerable constraints on the age and metallicity of the stellar population. Then, with age and metallicity in hand, we can use our synthetic CMDs to compare the predicted intrinsic color of the RGB with the observed color and thereby determine the reddening of the stellar population. At known reddening, the TRGB magnitude provides the galactic distance.

4.2. Age and Metallicity

In Fig. 8 we plot the observed LF of NGC 1569’s outer region as the solid black histogram with the completeness corrected LF plotted in red, where we have used our artificial star tests to determine the correction factor for each magnitude bin. Fainter than the TRGB (dashed vertical line), the LF of NGC 1569’s outer region shows a number of peaks, the most obvious of which is the RC/HB feature at $I \sim 28$. A comparison with the completeness corrected LF shows that we have only reached the bright end of the RC/HB, a result of the fact that NGC 1569 is 50% farther away than previously believed (§5.1). To determine which of the other peaks may be real features, in Fig. 8 we fit the slope of the RGB between $I = 24.8$ and 26.8 with a solid line. We also show error bars with the Poisson error for each magnitude bin. Although none of the other peaks along our LF are as conspicuous as seen by other authors (e.g., Rejkuba et al. 2005), there are two small bumps, marked with the arrows, that stick up above the RGB and are in the correct locations to possibly be the AGB and RGB bumps.

Having identified the RC/HB, as well as AGB and RGB bump candidates in NGC 1569’s LF, we can now compare the positions of these three features, plus that of the TRGB, to the predictions of theoretical isochrones. To measure the magnitudes of both bumps and the RC/HB in the observed LF of NGC 1569, we first subtract the slope of the RGB, leaving just the features in which we are interested. We fit gaussians to both bump features and take the center of the gaussian as the I -band magnitude of each feature. For the two bumps we find: $I_{bump1} = 26.94 \pm 0.02$ and $I_{bump2} = 27.12 \pm 0.03$, where the errors listed are the errors in the fit. Due to completeness issues near the RC/HB, which result in a steep drop off in the LF, fitting a gaussian to the RC/HB feature may yield a biased measurement. Instead, we simply take the magnitude of the LF bin with the most stars as our measurement of the RC/HB. For the RC/HB, which is ~ 0.4 mag wide (full width, zero intensity), or about eight times the LF bin size, we measure $I_{RC/HB} = 27.93 \pm 0.025$. This is an upper limit on the brightness of the RC/HB due to completeness effects. The quoted error is half the width of the magnitude bins in the LF. In §4.3 we discuss the measurement of the TRGB, for which we find $I_{TRGB} = 24.47 \pm 0.04$.

Due to the fact that our observations only reach down to the RC/HB branch feature, and not well below it, completeness and photometric errors may play a role in the magnitudes that we measure for the RC/HB and RGB and AGB bumps. Therefore, we cannot simply compare our numbers to those predicted by stellar evolution models. Instead, we use the same code as described below in Appendix A to create synthetic CMDs from each individual isochrone. In this, we make use of our artificial star test results to apply the appropriate errors and incompleteness. We have assumed a reddening of $E(B - V) = 0.56$ (Israel 1988), which, when combined with our measured TRGB value, gives a distance of ~ 3 Mpc. Then,

in the same way as for NGC 1569’s LF, we measure the magnitudes of the RGB bump, AGB bump, and RC/HB. At the brightness of the TRGB, completeness and errors are not expected to significantly affect our measurements. We therefore use the TRGB magnitude as reported in the isochrones.

Since then we are confident in our identification and measurement of the RC/HB, we use this feature to make the first cut in determining which age and metallicity best fits NGC 1569’s outer region. In Fig. 9 we plot the values of $I_{TRGB} - I_{RC/HB}$, as predicted by our synthetic CMDs, as a function of age for a range of abundances. Overplotted as the dashed line is our measured value for NGC 1569, with the dotted lines representing the 3σ error bars. Only those synthetic CMDs that fall within 3σ of our observed value are considered further. Because we have no *a priori* knowledge of the order of the AGB and RGB bumps, or if the bumps we have identified are actually real features, we consider all combinations of these two features in determining our best fit LF. We find that all of the best fit models for the RC/HB show only the AGB bump, with the RGB bump ‘lost’ in the RC/HB feature. The isochrone that provides the best fit to the positions of the TRGB, AGB bump, and RC/HB to within the measurement errors has $\log(\text{age}) = 10$ (10.0 Gyr) and $[\text{Fe}/\text{H}] = -1.4$ ($Z = 0.0008$). Its LF is plotted in Fig. 10 as the red histogram along with NGC 1569’s outer region (black histogram).

While this is the best fit model, there are two major differences between the observational data and model. First, the AGB bump and RC/HB features in the model are much more pronounced than what we observe. Second, the slope of the synthetic LF is similar to what is seen in star clusters ($N(L) \propto L^{-\beta}$ with $\beta \approx 0.32$; e.g., Zoccali & Piotto 2000) whereas the slope of NGC 1569’s RGB is much steeper ($\beta = 0.37$). The poor fit to the bump features opens the possibility that the bumps we have identified in the LF in Fig. 8 may not be associated with the actual RGB and AGB bumps in NGC 1569. That is not to say that they do not exist in NGC 1569, but rather that they have been smoothed out due to a superposition of mixed stellar populations. Combined with the difference between predicted and observed LF slopes, this suggests that NGC 1569’s LF as a whole is not represented by any single age, single metallicity population; it must have had a more complex SFH, which we derive explicitly in §5.

4.3. Distance and Reddening

As discussed in Grocholski et al. (2008), our data represent the first unequivocal detection of the TRGB in NGC 1569 and thereby allow us to determine its distance via the luminosity of the TRGB. Although we presented the distance to NGC 1569 in Grocholski et al.

(2008), since we have reprocessed our data using the most recent HST ACS calibration data we revisit our distance calculation, which also depends on the reddening. We calculate the distance and reddening here, still assuming NGC 1569 can be represented by a SSP, and discuss the results from more complicated SFHs in §5.2.

In the LF of a stellar population the TRGB acts as a discontinuity, the position of which is easily measured. Using the software developed by one of us (R. P. v. d. M.) and detailed in Cioni et al. (2000), we find that $I_{TRGB} = 24.47 \pm 0.04$. The location of the TRGB is marked by the vertical dashed line in Fig. 8. We note that this value is slightly fainter than reported in Grocholski et al. (2008) due to the updated processing and photometry.

For the reddening appropriate for NGC 1569, we can either use values from the literature (as we did in Grocholski et al. 2008), or we can estimate it from our data. Literature values for the foreground extinction toward, and intrinsic reddening in, NGC 1569 span a wide range of values. The most commonly adopted value is $E(B - V) = 0.56$ (Israel 1988), which was calculated using integrated UV photometry of the core of NGC 1569. Since the recent star formation, and therefore the gas and dust, in NGC 1569 is concentrated in the core, we expect the reddening in the outer region to be lower. Thus, in Grocholski et al. (2008) we adopted the foreground extinction due to the Milky Way provided by the Burstein & Heiles (1982) reddening map, $E(B - V) = 0.50$. We note that the reddening map of Schlegel et al. (1998) gives a much higher value, $E(B - V) = 0.68$, for NGC 1569. However, as discussed by Relaño et al. (2006), this estimate of the *foreground* extinction is higher than the *total* extinction in NGC 1569 derived by many authors (e.g. Israel 1988, Origlia et al. 2001) suggesting that it is likely an overestimate of the reddening at the position of NGC 1569.

In the previous section we used the relative brightnesses of the TRGB, AGB bump, and RC/HB features to determine an estimate for the age and [Fe/H] of the dominant population in NGC 1569. Since the RGB spans a very small range in color, this approach gives an age and metallicity that is independent of the reddening of the stellar population. Thus, to determine $E(B - V)$ from our data we can compare the observed RGB color of NGC 1569 with that predicted for a synthetic population that has an age of 10 Gyr and [Fe/H] = -1.4. For RGB stars on the synthetic CMD ~ 0.5 mag below the TRGB, we find an intrinsic color of $(V - I)_0 = 1.29$. Over the same magnitude range, RGB stars in NGC 1569’s outer region have an average apparent color $(V - I) = 1.98$. This implies a reddening of $E(B - V) = 0.58$ (adopting the reddening law of Cardelli et al. (1989), where $A_V = 3.1E(B - V)$ and $A_I = 0.614A_V$ for photometry on the Johnson-Cousins system).

The absolute I -band magnitude of the TRGB (M_I^{TRGB}) is well known to be roughly constant around ~ -4.0 mag in SSPs with age $\gtrsim 2$ Gyr and [Fe/H] $\lesssim -0.5$. Barker et al. (2004) used synthetic CMDs to study the reliability of the TRGB as a standard candle for resolved

stellar populations with complex SFHs. They found that $M_I^{TRGB} = -4.0 \pm 0.1$ independent of the SFH, provided that the median dereddened color of RGB stars ~ 0.5 mag below the TRGB is $(V - I)_0 \lesssim 1.9$. It is therefore appropriate to assume $M_I^{TRGB} = -4.0 \pm 0.1$ for our distance calculations. Combined with $I_{TRGB} = 24.47 \pm 0.04$ and $E(B - V) = 0.50 \pm 0.05$ (from Burstein & Heiles 1982), this yields $(m - M)_0 = 27.52 \pm 0.14$ or $D = 3.19 \pm 0.21$ Mpc. If we instead use the reddening estimated from our RGB analysis, $E(B - V) = 0.58 \pm 0.06$ (we assume a 10% error), we find $(m - M)_0 = 27.36 \pm 0.16$ or $D = 2.96 \pm 0.22$ Mpc. Both of these distances are much farther than the typically assumed distance of 2.2 Mpc (e.g., Israel 1988) and place NGC 1569 on the near edge of the IC 342 group of galaxies.

5. Star Formation History Extraction from the CMD

5.1. Methodology

We showed in §4 that the LF of the NGC 1569 outer region is not well fit by an SSP and must have had a more complex SFH. To infer this SFH we use the new SFHMATRIX code (van der Marel & Grocholski in prep.) described in Appendix A. Starting from a set of isochrones, and for any assumed distance and extinction, the code finds the SFH as function of age and metallicity that best matches the Hess diagram of the observed CMD in a χ^2 sense. We note that the full SFH calculations are independent of our SSP analysis and that the accuracy of our SFH is ultimately tied to the accuracy of the stellar evolution models we have adopted.

For a given assumed extinction, we find the best-fitting distance as follows. We start with a trial distance and find the best fitting SFH. From this we create a synthetic CMD realization (i.e., a Monte-Carlo realization that has the same number of stars on the CMD, taking incompleteness and photometric errors into account, as the observed CMD). We then analyze both the observed and the synthetic CMD with the TRGB analysis software described in Section 4.3. Based on the inferred difference between the observed and synthetic TRGB magnitudes we adjust the trial distance, and iterate this procedure till convergence (agreement better than 0.01 mag). The iteration is necessary because not all SFHs yield the same absolute TRGB magnitude; the distance depends on the SFH. There generally is agreement at the ± 0.1 mag level (e.g., Barker et al. 2004), but this is not sufficient for the most accurate results.

To infer the extinction, we run the procedure for a range of trial extinction values and plot the χ^2 of the CMD fit as a function of extinction (see Fig. 11). The data vary smoothly and are well fit by a fourth-order polynomial (dashed curve). This has a minimum

at $E(B - V) = 0.58$, which provides the best-fitting extinction. The corresponding best-fitting distance modulus is $(m - M)_0 = 27.43$, yielding a distance of 3.06 Mpc. These results agree very well with published reddenings as well as the results from our SSP analysis of the LF and RGB color in Section 4.3. In principle, the random errors on the extinction and distance can be robustly determined using a repeated analysis of pseudo-data created from the observed CMD data set using bootstrapping (see Appendix A). In practice, systematic errors of various kinds are probably of more importance. Based on the combined insights from literature studies of the extinction, and our own SSP and SFH analyses, we adopt as our final estimates $E(B - V) = 0.58 \pm 0.03$ and $D = 3.06 \pm 0.18$ Mpc. The distance error is dominated by the systematic uncertainty in the knowledge/calibration of the absolute magnitude of the TRGB feature.

It is of interest to note that the SFH analysis yields extinction values that are consistent with those inferred through independent techniques. This means that the CMD data has enough information content to break the age-metallicity-extinction degeneracy for old populations. The color and curvature of the RGB is driven primarily by metallicity with only a small contribution from age. Metal-poor isochrones are relatively blue with little curvature, while metal-rich isochrones are red and have a significant amount of curvature. Therefore, if we use too low of a value for the extinction, the SFH code must use the metal-rich isochrones to match the observed color of the RGB, resulting in a synthetic CMD with too much curvature on the RGB. Conversely, high values of extinction lead to metal-poor synthetic CMDs with too little RGB curvature. Since our data reach ~ 4 mag below the TRGB, the curvature is observationally well constrained. We found that the high χ^2 values in Fig. 11 for models with relatively low or high extinction values are driven in part by the fact the models for these extinctions cannot fit the observed RGB curvature at the given (observed) color.

5.2. The CMD Fit

Fig. 12 compares the observed CMD (right) to a synthetic CMD realization (left) from the best-fit SFH. The area below the solid line was excluded from the χ^2 minimization because the completeness is below 20% there, making the artificial star corrections unreliable. The area above and to the right of the dashed box was also excluded, for two reasons. First, this is where foreground stars are found (see Fig. 4), which are not explicitly accounted for in our models. Second, this is where thermally pulsating AGB (TP-AGB) stars are located. Near the end of their AGB lifetimes, these stars undergo a series of He shell flashes due to the He- and H-burning shells turning on and off. While the updated Padova models

(see Girardi et al. 2010) provide a much improved treatment of the TP-AGB stars, this is still a complex and highly uncertain phase of stellar evolution. Moreover, a significant but unknown fraction of TP-AGB stars may be obscured by dust shells (Boyer et al. 2009) making it difficult to use such stars to constrain the SFH.

In the region of the CMD that was fitted, the agreement between the synthetic and observed CMDs is excellent. The χ^2 of the fit is 2668, for $N_{\text{DF}} = N_{\text{pix}} - N_{\text{basis}} = 898$ degrees of freedom. Here $N_{\text{pix}} = 1773$ is the number of pixels in the CMD Hess diagram that was fitted, and $N_{\text{basis}} = 875$ is the number of different (isochrone) basis functions that was used to build the fit. The ratio $\chi^2/N_{\text{DF}} = 2.97$ is somewhat higher than expected purely from random errors, but such ratios are not atypical for studies of this kind (McQuinn et al. 2010). The only visually obvious discrepancies between the synthetic and observed CMDs occur in the regions that were masked in the fit. These discrepancies are well-understood: shortcomings in the TP-AGB evolutionary models at bright magnitudes and shortcomings in the correcting of very incomplete data with artificial start tests at faint magnitudes. These do not impact the inferred SFH, because of the exclusion of these regions from the fit.

Fig. 13 compares the LF of NGC 1569 (*black*) to the model LF for the best-fit SFH (*red*). As described above, there are well-understood discrepancies brighter than the TRGB (arrow) and fainter than $I \gtrsim 28$. However, at the intermediate magnitudes that were actually included in the χ^2 minimization, the fit is excellent. This is particularly true when compared to the predictions of the best-fit SSP in Fig. 10. The best-fit SFH shows excellent agreement with the observed slope of the RGB, the observed magnitude and prominence of the RC/HB, and the lack of other prominent features (e.g., the RGB and AGB bumps).

Fig. 13 compares the LF of NGC 1569 (*black*) to the model LF for the best-fit SFH (*red*). As described above, there are well-understood discrepancies brighter than the TRGB (arrow) and fainter than $I \gtrsim 28$. However, at the intermediate magnitudes that were actually included in the χ^2 minimization, the fit is excellent. The best-fit SFH matches the observed slope of the RGB, the observed magnitude and prominence of the RC/HB, and the lack of other prominent features (e.g., the RGB and AGB bumps). This is in sharp contrast to our best fit SSP in Fig. 10, and confirms our assessment in § 4.2 that NGC 1569 is not well fit by any SSP and must have had a more complex SFH.

5.3. Star Formation History

Fig. 14 shows the full SFH of NGC 1569’s outer region as a color-contour plot as a function of $\log(\text{age})$ and $[\text{Fe}/\text{H}]$. The quantity that is plotted is the predicted number of

stars on the unmasked portion of the CMD. Thus, this provides a direct assessment of which (age,metallicity) combinations contribute most to the observed CMD. The SFH shows a number of salient features, which we will discuss in turn.

(1) The peak of the SFH is found at old ages ($\log(\text{age}) \gtrsim 10$) and metallicities from $[\text{Fe}/\text{H}] = -1$ to -2 , but centered around $[\text{Fe}/\text{H}] = -1.25 \pm 0.1$. This is very similar to the properties of the best-fit SSP inferred in §4.2, which has $\log(\text{age}) = 10.0$ and $[\text{Fe}/\text{H}] = -1.4$ (open star in Fig. 14). There is a well-known age-metallicity degeneracy in the modeling of old stellar populations. Before accepting a SFH result, one must therefore ask if the age-metallicity dependence of the inferred SFH is uniquely implied by the data, and if the data did indeed have the information content necessary to ameliorate the degeneracy. In this case, the answer is yes. We have tried to match our observations of NGC 1569 using basis functions with restricted parameter space [e.g., $\log(\text{age}) \leq 9.9$ (8 Gyr)], but find that with these restrictions we cannot match the observed LF. Thus, while the precise age and metallicity of stellar populations can only be determined through a combination of spectroscopy and MSTO photometry, the information available on the RGB (brightness of the TRGB and RC/HB, color and curvature of the RGB) is sufficient to prefer a predominantly old population with a spread in metallicity.

(2) The SFH shows a general trend of younger stars having higher metallicities. The metallicity of the gas in the central regions of NGC 1569 has been measured to be $[\text{Fe}/\text{H}] = -0.6$ (dashed horizontal line in Fig. 14). There are few stars in the SFH model at metallicities higher than this, and the youngest stars inferred with significance ($\log(\text{age}) \approx 8.7$) have a metallicity that approaches this value. This is all as generically expected in scenarios of chemical evolution. Younger stars formed from gas that was pre-enriched by the ejecta of older stars, and the youngest stars should have metallicities similar to that of the gas. These results therefore also provide additional credibility for the SFH results.

(3) Even though the CMD only shows a predominant RGB, the SFH actually has significant star formation in the outer region for the age range from approximately 0.5 – 2.0 Gyr ago ($\log(\text{age})$ between 8.7 and 9.3). Since this may appear counter-intuitive, it is important to understand why this occurs in the models. The luminosity at the TRGB, i.e. the point of central He ignition, is virtually constant with increasing stellar mass, up to close to the *RGB phase transition* mass. Stars that are less massive than the phase transition mass have fully degenerate cores when they begin He fusion, while He ignition occurs in more massive stars under non-degenerate conditions (Sweigart et al. 1990). As stars approach this transition mass, the luminosity of the TRGB rapidly decreases by ~ 2 mag in the *I*-band. In terms of age, the RGB phase transition occurs in the Padova isochrones at ~ 1 -2 Gyr, with the younger, more massive stars populating a short RGB, while the older, less massive

stars form the fully extended RGB. Our observed RGB luminosity function can only be reproduced with an intermediate age component, which steepens the LF by populating the magnitude range $27 \lesssim I \lesssim 28$, on top of the extended RGB component provided by the older stellar populations. This argument is illustrated in Fig. 15 where we plot the synthetic CMD realization from the best-fit SFH, broken down into its age (*left*) and metallicity (*right*) components.

(4) The *observed stars* in the outer region span a range of ages, from ~ 0.5 Gyr to a Hubble time (Fig. 14). However, the *mass* in the outer region resides almost exclusively in the oldest stars. As a population ages, the fraction of the stars that is observable decreases. Therefore, a single observed star that is old hints at a much larger underlying reservoir of unseen stars than does a star that is younger. For the best-fit SFH, 93% of the total outer region mass resides in stars with $\log(\text{age}) \geq 9.7$ (age > 5 Gyr).

(5) Even the oldest stars have a significant spread in metallicity, ranging between $[\text{Fe}/\text{H}] = -1$ and -2 . This is evident from Fig. 16, which shows the distribution of stellar mass vs. $[\text{Fe}/\text{H}]$, for only those stars with $\log(\text{age}) \geq 9.7$. The error bars indicate that the individual peaks and valleys seen as a function of metallicity in this range are probably not statistically significant, with the possible exception of a dip around -1.8 dex. However, the spread in metallicity is a persistent feature of the various SFH fits we have explored. This is due to the observed RGB width, which exceeds the photometric errors, and therefore requires a metallicity spread to be reproduced by the SFH code. Note that the total mass in the field under study is small, because we are looking at a low density field in the outer region. The integral under the histogram in Fig. 16 corresponds to only $5.0 \times 10^7 M_\odot$. The spread in $[\text{Fe}/\text{H}]$ in NGC 1569’s outer region is similar to that of the Milky Way halo; using SDSS data, Ivezić et al. (2008) find that the Milky Way halo metallicity distribution is well fit by a gaussian with $[\text{Fe}/\text{H}] = -1.46$ and an intrinsic width, $\sigma = 0.30$.

(6) After most of the outer region stars formed early in the Universe ($\log(\text{age}) \geq 9.7$), NGC 1569 experienced a relatively constant rate of star formation until ~ 0.5 Gyr ago. Fig. 17 shows the star formation rate (SFR; expressed in M_\odot/yr) as function of $\log(\text{age})$ (integrated over all metallicities). The error bars indicate that the increase in SFR some ~ 0.5 Gyr ago ($\log(\text{age}) \geq 8.7$) may be statistically significant, but not necessarily so. The oldest epoch of star formation in NGC 1569’s outer region is congruent to that of the Milky Way globular clusters, which formed from the earliest times up until about 7 Gyr ago (Marín-Franch et al. 2009). This is also similar to the Λ CDM simulations of a Milky Way-like halo by Font et al. (2006), which showed that 80% of the mass in the inner halo ($R < 20$ kpc) was accreted by ~ 9 Gyr ago, with almost no mass ($\ll 1\%$) assembled in the last 5 Gyr. For reference, at the distance of NGC 1569, the full ACS field-of-view is ~ 3.1 kpc

$\times 3.1$ kpc. In contrast to the oldest stars, the extended formation of stars in NGC 1569’s outer region until 0.5 Gyr ago is inconsistent with the formation scenarios of the Milky Way halo, indicating that NGC 1569 likely had atypical environmental influences (see §6).

(7) The outer region of NGC 1569 does have a few young stars. The sparsely populated CMD plume at $V - I \approx 0.4$ (see Fig. 3) is fit by the SFH code as a low level of star formation at ages $\lesssim 30$ Myr. It is possible that these stars may have formed closer to the core of the galaxy, followed by outward migration through dynamical processes. To travel from the galaxy center to the outer region in 30 Myr requires a transverse velocity of ~ 50 km/s, which is not out of the question.

5.4. Core-Outer Region SFH Comparison

We have focused here on a study of the SFH of the NGC 1569 *outer region*. It is of interest to see how our results compare to those previously derived by other authors for the *core* of the galaxy. The most recent analysis of this was performed by McQuinn et al. (2010). They used a subset of our ACS images, performed their own photometry and determined the SFH of NGC 1569 via CMD fitting with MATCH. Similar to us, they assumed a Salpeter IMF and used the Padova stellar evolution models. Because of uncertainties due to the extreme crowding and differential reddening in the central region of the galaxy, McQuinn et al. (2010) required that $[\text{Fe}/\text{H}]$ increases with time. While our analysis allows more general chemical evolution, the inferred SFH for the outer region is in fact generally consistent with an increasing $[\text{Fe}/\text{H}]$ with time. The published McQuinn et al. (2010) SFH refers to the entire ACS field.⁴ Since the stars and mass of NGC 1569 are heavily concentrated towards the galaxy core, that region carries almost all the weight in their SFH. For simplicity, we’ll refer to their result as the SFH of the core.

In Fig. 17 we compare our outer region SFR as a function of age (top panel) to the core SFR from McQuinn et al. (2010, bottom panel). Of course, the core SFR is significantly enhanced at young ages compared to what is seen in the outer region. But for the more ancient populations, our studies are in good overall agreement: most of the old stars formed ~ 10 Gyr ago; a low but significant amount of star formation persisted between 1 and 10 Gyr ago; and there was a SF peak/burst at ~ 0.3 – 0.7 Gyr ago. The similarity between the outer region and core SFHs for old stars implies that there are no strong radial population

⁴McQuinn et al. (2010) divided the galaxy into low and high surface brightness regions, which is likely similar to our core/outer region distinction. Their published SFH is the sum of the individual SFRs for the low- and high-surface brightness regions.

gradients for the old stars. This is also consistent with our recent study in Rys’ et al. (2011) of HST/WFPC2 parallel fields much further out in the outer region. Out to 8 scale radii, we detected no variation in either RGB color or carbon-to-RGB star count ratio in the outer region. In view of these results, the results for our outer region can be taken to be representative of the old stellar populations throughout the galaxy.

As with SFHMATRIX, MATCH can be used to determine the best fit distance and reddening of the galaxy. For the high surface brightness region, McQuinn et al. (2010) find a best fit distance of 3.2 ± 0.1 Mpc and $E(B - V) = 0.58 \pm 0.03$, similar to what we find for the outer region (see §5.1). However, for the low surface brightness region, which should be similar to our outer region, they find a larger distance, 3.5 ± 0.1 Mpc, and lower reddening, $E(B - V) = 0.48 \pm 0.04$, than we calculate for the outer region. The source of this discrepancy is unclear, but is possibly due to a difference in photometric depth. As we discussed in §4.3, reaching fainter features on the RGB LF helps to ameliorate the degeneracy between age, metallicity, and reddening. Our outer region LF (Fig. 8) shows that we barely reach the RC/HB in NGC 1569. McQuinn et al. (2010), on the other hand, use only a subset of our data. A comparison of their published CMD of the entire NGC 1569 field (their Fig. 3) with our CMD of the core (see Fig. 2) shows that our photometry reaches 0.5 - 0.75 mag deeper. Thus, their calculation of the reddening and distance does not benefit from the added constraints provided by the RC/HB. It is interesting to note, however, that even though McQuinn et al. (2010) do not reach the same photometric depth as we do, their SFH is very similar to ours. This suggests that even without the RC/HB feature a significant amount of information can still be gleaned from the CMD.

6. Possible Star Formation Triggers

The central region of NGC 1569 is currently undergoing a strong starburst. Our CMD analysis of its outer region indicates that a constant level of star formation has been maintained there for much of the Hubble time. This prompts the question of what may have triggered this star formation activity.

Its projection on the sky places NGC 1569 near the IC 342 group. The IC 342 group is comprised of nine known galaxies and has a mean distance of 3.35 ± 0.09 Mpc, with a line-of-sight depth of 0.25 Mpc (1σ ; Karachentsev 2005). NGC 1569 was long assumed to lie only 2.2 Mpc away (e.g., Israel 1988), placing it in a relatively isolated position between the Local Group and the IC 342 group. However, the TRGB distance inferred from our HST data, $D = 3.06 \pm 0.18$ Mpc, places NGC 1569 inside the IC 342 group, raising the possibility that interactions with the group or its galaxies may have triggered the star formation in

NGC 1569 (Grocholski et al. 2008).

In the rest frame of the Local Group, the IC 342 group (excluding NGC 1569 and UGCA 92, see below) has a line-of-sight velocity $\langle V_{LG} \rangle = 226 \pm 18 \text{ km s}^{-1}$, with a dispersion of 54 km s^{-1} (Karachentsev 2005). NGC 1569 has a lower velocity, $V_{LG} = 88 \text{ km s}^{-1}$, that is 2.5σ from the group average. So NGC 1569 may reside in the tail of the velocity distribution of the IC 342 group, or it may not be bound to it at all (depending on its unknown transverse velocity, v_{trans}).

Since NGC 1569 lies at the front side of the IC 342 group, NGC 1569 is now moving away from it. Given the known line-of-sight velocities and distances, we can calculate that it was at the same distance as the IC 342 group ~ 2.1 Gyr ago, and entered the far side of the IC 342 group ~ 3.8 Gyr ago. Fig. 17 shows that the NGC 1569 outer region had a relatively constant non-zero star formation rate in this period. Thus, interactions with the IC 342 group, whether from tidal forces between galaxies or through ram pressure compression by IGM gas may have played a role in its SFH.

It is possible that NGC 1569 may have interacted strongly with a particular galaxy in the IC 342 group. One candidate is the dwarf galaxy UGCA 92. Like NGC 1569, UGCA 92 has a distance of ~ 3 Mpc and $V_{LG} = 89 \text{ km s}^{-1}$ (Karachentsev et al. 2006). They are separated on the sky by only $1^{\circ}23'$, which gives a physical distance of ~ 65 kpc. A recent study by Jackson et al. (2011) shows that NGC 1569 is sitting in a large, cold HI cloud, with tidal tails stretching out toward UGCA 92. The combination of small spatial separation, similar line-of-sight velocity, and the HI gas possibly connecting the two galaxies suggests that NGC 1569 and UGCA 92 may be interacting with each other. It is therefore possible that tidal forces between these galaxies have driven the long term SFH of both galaxies. Dynamical models have shown that close encounters between two dwarf galaxies, such as the Magellanic Clouds, can lead to widespread star formation (e.g., Bekki et al. 2004; Besla et al. in prep.). However, the distance between NGC 1569 and UGCA 92 is about three times the current separation between the Magellanic Clouds. In absence of knowledge about v_{trans} , it is not possible to know whether NGC 1569 may have interacted directly with IC 342 itself. Also, the distance to IC 342 is not particularly well known, with many widely separated values quoted in the literature (e.g., Tikhonov & Galazutdinova 2010; Saha et al. 2002 and references therein).

7. Summary and Conclusions

NGC 1569 is one of the closest and strongest starburst galaxies in the Universe. While its ISM and recent star formation have been thoroughly studied, until recently, little was known about NGC 1569’s old stellar populations. This has made it difficult to determine the exact duration of the starburst, to unravel its triggers, and to understand NGC 1569’s evolution over a full Hubble time. For this reason, we used HST/ACS to obtain deep V - and I -band images that reach down to $M_V \sim -0.5$. These data allowed us to show definitively for the first time that NGC 1569 has a significant population of stars older than 1 Gyr (Grocholski et al. 2008). Here we have used the same data to derive the properties and full SFH of this old population.

We focused our analysis on the outer region of the galaxy, which is largely devoid of young stars and is much less crowded than the core. The improved photometric depth provides access to the RC/HB, which helps to ameliorate the age-metallicity degeneracy that plagues SFH studies that focus only on the RGB. We have used first an approach based on simple stellar populations. We then presented a newly developed synthetic CMD fitting code, SFHMATRIX, and used it to determine the full SFH. By combining the results from the different approaches, we were able to derive the following coherent picture for NGC 1569’s old stellar populations.

(1) By treating NGC 1569’s outer region as an SSP, we find that the relative brightnesses of observed LF features (TRGB, RC/HB, and AGB bump) are best matched by a SSP with age = 10 Gyr and $[\text{Fe}/\text{H}] = -1.4$. However, the model SSP LF slope is flatter and the features more pronounced than what we observe in NGC 1569. This discrepancy suggests that NGC 1569 cannot be treated as an SSP as it must have had a more complex SFH.

(2) The distance/reddening combination that best fits the data with a full SFH analysis is $E(B - V) = 0.58 \pm 0.03$ and $D = 3.06 \pm 0.18$ Mpc. The reddening is in agreement with values published using other techniques, but the distance is $\sim 50\%$ farther than what has been typically assumed.

(3) Star formation in the outer region of NGC 1569 began ~ 13 Gyr ago and lasted until ~ 0.5 Gyr ago. The majority of star formation in our observed field occurred early on, with 93% of the stars, by mass, having formed more than 5 Gyr ago. This initial burst was followed by a relatively low, but constant, rate of star formation until ~ 0.5 - 0.7 Gyr ago when there may have been a short, low intensity burst of star formation.

(4) The SFH for the old population in the NGC 1569 outer region follows a trend of increasing metallicity with time. The youngest significant population of ~ 0.5 - 0.7 Gyr age has a metallicity similar to that of the ionized gas in NGC 1569. These results are consistent

with the basic expectations of chemical evolution scenarios.

(5) NGC 1569’s dominant old population (age $\gtrsim 10$ Gyr) shows a considerable spread in metallicity, ranging from $[\text{Fe}/\text{H}] = -1$ to -2 , with a peak around $[\text{Fe}/\text{H}] = -1.25$. The mean of this distribution is very similar to what we derived in our SSP analysis. The metallicity-spread of the dominant old population is similar to that for the Milky Way halo. However, the star formation in NGC 1569’s outer region extended for much longer than in the Milky Way, indicating that NGC 1569 likely had atypical environmental influences.

(6) The distance and line-of-sight velocity of NGC 1569 indicate that it moved through the IC 342 group of galaxies, at least in the past few Gyr. This may be the reason for the extended low-level star formation seen in its outer region. By contrast, its recent starburst may be related to interactions with the companion UGCA 92.

(7) Comparison with recent work from McQuinn et al. (2010) and Ryś et al. (2011), which was more heavily weighted towards smaller and larger radii in the galaxy, respectively, provides no evidence for radial population gradients in the old population of NGC 1569. This suggests that our results for the outer region are representative for the old stellar population throughout the galaxy.

We would like to thank Jay Anderson for helpful discussions regarding early versions of the photometry, Leo Girardi for answering many questions about the Padova models, and Kristen McQuinn for kindly providing an electronic version of her SFH for NGC 1569. The authors would also like to thank the anonymous referee for comments that helped to improve the clarity of the paper. We are grateful to Jennifer Mack, Luca Angeretti, Enrico Held, Donatella Romano and Marco Sirianni for collaboration on earlier stages of this project. Support for proposal GO-10885 was provided by NASA through a grant from STScI, which is operated by AURA, Inc., under NASA contract NAS 5-26555. F.A. and M.T. acknowledge partial financial support from ASI through contracts ASI-INAF I/016/07/0 and I/009/10/0.

Facility: HST (ACS).

A. Star Formation History Analysis with SFHMATRIX

The Star Formation History (SFH) of a galaxy can be described mathematically as a sum of delta functions. Each delta function has a fixed combination of age and metallicity, and a weight corresponding to the mass of stars that formed with that combination. This implies that the CMD of a galaxy can be described as the weighted linear sum of a set

of “basis functions”, where each basis function corresponds to the synthetic CMD for an isochrone with fixed age and metallicity (Tosi et al. 1991). The basis functions must reflect the characteristics of the problem at hand, namely: (1) observational details, such as the completeness and photometric errors inferred from artificial star tests; (2) galaxy properties, such as the distance and total (foreground+internal) extinction; and (3) stellar population properties, such as the Initial Mass Function (IMF) with which an isochrone is populated, and the binary fraction.

Framed in this manner, the problem of inferring the SFH of a galaxy from its CMD reduces to the problem of finding the weighted combination of synthetic basis function CMDs that best reproduces the observed CMD. Since the data consist of a discrete set of points, this can be expressed mathematically as a maximum likelihood problem (e.g., Dolphin 2002). However, when the number of basis functions is large, such problems can be complicated to solve numerically. It is therefore advantageous to consider instead the density of points in the CMD, i.e., the Hess diagram, rather than the CMD itself (both for the observations and the basis functions). By pixelating the CMD and assigning an appropriate error bar to the observed density in each pixel, the problem reduces to a linear χ^2 minimization problem (e.g., Harris & Zaritsky 2001). For large numbers of stars, these approaches become mathematically equivalent due to the central limit theorem.

Many software implementations have been developed to infer the SFH from an observed CMD, mostly using approaches similar to those outlined above (see, e.g., the compilation and comparison of various methods described in Skillman & Gallart 2002). Here we use a new code that we developed, called SFHMATRIX. We describe here the salient features, with a more detail description planned for a separate paper (van der Marel & Grocholski in prep.). Our code resembles the STARFISH code of Harris & Zaritsky (2001). Our method of constructing a synthetic CMD from an isochrone is largely similar to theirs, and like STARFISH, we describe the problem mathematically as a χ^2 minimization.

Our code differs primarily from the STARFISH implementation in how it finds the χ^2 minimum, i.e., the best-fitting SFH. STARFISH finds the minimum using a brute-force minimization in N -dimensional space, where N is the number of basis functions (i.e., the number of different isochrone weights to be optimized). By contrast, we phrase the problem as the solution of a matrix equation (hence the name “SFHMATRIX”)

$$\sum_{j=1}^N A_{ij} m_j = \rho_i \pm \Delta\rho_i, \quad \forall i = 1, \dots, M \quad . \quad (A1)$$

Here ρ_i is the density of the stars in CMD space, $\Delta\rho_i$ is the associated Poisson uncertainty, and the index i counts the M pixels of the Hess diagram. The density ρ_i equals the integer

number of stars $L_i \geq 0$ that is detected in Hess diagram pixel i , divided by the area of that pixel. We adopt $\max(1, \sqrt{L_i})$ as the Poisson error on the detected number of stars. Hence, $\Delta\rho_i/\rho_i = \max(1, \sqrt{L_i})/L_i$. The vector of weights $m_j \geq 0$ gives the mass (in M_\odot) of stars associated with the N basis functions (i.e., isochrones) j . The matrix A_{ij} gives the density of stars in Hess diagram pixel i for a $1M_\odot$ population of stars on synthetic isochrone j . Finding the solution of this matrix equation is a non-negative least squares (NNLS) problem in linear algebra. This can be solved with efficient general purpose subroutines (e.g., Lawson & Hanson 1974) that have been well tested in other areas of astronomy (e.g., the dynamical modeling of galaxies using Schwarzschild’s orbit superposition technique; e.g., van der Marel et al. 1998).

Our approach has several advantages over the STARFISH approach. First, the NNLS matrix routines are guaranteed to converge on a global minimum (Lawson & Hanson 1974), and cannot inadvertently find local minima as do brute-force searching routines. Second, the speed of NNLS routines makes it easy to use many basis function (large N), so that it is possible to effectively search and characterize the space of relevant models on a fine grid (both in age and metallicity, as well as in other parameters such as extinction and distance). Third, the speed of NNLS routines makes it easy to run the code in Monte-Carlo sense on many simulated datasets, so that the uncertainty on the final SFH can be robustly characterized.

Our code can create basis functions from any set of isochrones. It is important that the basis functions fully span the range of ages and metallicities that are relevant for the galaxy under study. It is also important that the spacing between adjacent isochrones is relatively fine. If it is too coarse, then a fitted CMD superposition looks choppy and discontinuous in those regions of CMD space where the observational errors are small. On the other hand, the computational effort of the NNLS solution scales with the number of basis functions as N^3 . So it is best not to choose more basis functions than can realistically be resolved by the data given the observational errors.

Here we use the isochrones from the same Padova models as discussed in §4 and we note that these are the same isochrones used in the paper by McQuinn et al. (2010). We use metallicities ranging from -2.28 dex to +0.20 dex and $\log(\text{age})$ values from 6.60 to 10.12. We obtained isochrones spaced by 0.05 dex in metallicity and 0.01 dex in $\log(\text{age})$. Most of these isochrones are obtained from interpolation between a much coarser set of isochrones (in particular in metallicity) for which actual stellar evolutionary calculations were performed (e.g., Fagotto et al. 1994a,b). We created synthetic CMDs from each basis function by randomly drawing many stars from the isochrone, given an assumed IMF, and then rescaling the corresponding Hess diagram density to correspond to $1M_\odot$. Stars are

assigned a simulated photometric error and are marked as either detected or not (thus accounting for incompleteness) based on a randomly drawn artificial star from the artificial star test results. To construct basis functions that are not sampled quite as finely, we co-add the synthetic CMD results within bins of size 0.1 dex in metallicity and 0.1 dex in $\log(\text{age})$.⁵

Finding the best-fitting SFH from an observed CMD is mathematically an inverse problem. Methods for solving such problems have the well-known tendency for amplifying noise, leading to solutions that appear unphysically spiky. This can be counteracted by enforcing smoothness on the solution. Regularization is one popular technique for doing this (e.g., Press et al. 1992). In the context of NNLS solutions, linear regularization constraints can be enforced by adding K additional rows of the following form to the matrix equation

$$\sum_{j=1}^N B_{kj} m_j = 0 \pm \Delta, \quad \forall k = 1, \dots, K \quad . \quad (\text{A2})$$

(see Cretton et al. 1999). The B_{kj} are chosen such that for given k , the expression $\sum B_{kj} m_j$ is a second order divided difference of basis functions that are adjacent in age at fixed metallicity, or vice versa. The divided differences are zero if the SFH is locally well approximated by a linear function. In this manner, smoothness is enforced in (age,metallicity) space, with the exact amount depending on the parameter Δ . If $\Delta = \infty$, then the regularization constraints are ignored. If $\Delta = 0$, then the data are ignored, and the code cares only about returning a smooth solution. For intermediate values, the NNLS solutions tries to fit the data as best as possible, while keeping the noise in the SFH in check. In practice we applied a small amount of regularization to obtain the results in this paper, but none of our main results depend sensitively on this.

Calculating error bars on the best-fitting SFH returned by the code is straightforward. For this we create many realizations of pseudo datasets with properties similar to the real data. We analyze each of these pseudo datasets in Monte-Carlo fashion as we do the real data. The RMS scatter in the SFH results at a given (age,metallicity) combination is the error bar. The pseudo data can be created with either of two possible approaches. The first approach is to use bootstrapping (Press et al. 1992). In this approach one obtains a new dataset of S stars from the existing dataset of S stars, by random drawing with replacement. The second approach is to use the best-fitting SFH already inferred from the real data, and to draw many Monte-Carlo pseudo dataset realizations from this SFH. In the present paper we use the bootstrapping approach to calculate SFH error bars.

⁵This results in each basis function corresponding to a two-dimensional comb function that approximates a two-dimensional boxcar. The resulting SFH is therefore more akin to a two-dimensional histogram, than a sum of delta-functions.

To test the accuracy of the code we explored two approaches. In the first approach we used pseudo dataset realizations drawn from a known SFH, and then used the code to verify that the inferred SFH agrees with the input SFH to within the errors. In the second approach we used our code and the publicly available STARFISH code on the same input data, and verified that the inferred SFHs agreed to within the errors. Both tests were passed successfully.

We also explored the sensitivity of the results to the small changes in the stellar evolutionary models using two approaches. In the first approach we used our code with either the isochrones from Bertelli et al. (1994) or Girardi et al. (2002) to infer the SFH from the same data. In the second approach we used our code with basis functions that were created either from the Bertelli et al. (1994) isochrones, or directly from the Fagotto et al. (1994a,b) evolutionary tracks from which these isochrones were derived, and then derived the SFH from the same data. The approaches all yielded results in satisfactory agreement. However, more generally this does depend on both the actual differences in the underlying evolutionary calculations, and the characteristics and quality of the available data. Different stellar evolutionary tracks can yield different implied SFHs when used to analyze the same data (e.g., Skillman & Gallart 2002).

We have assumed a Salpeter IMF (Salpeter 1955) from $0.1 - 100 M_{\odot}$ in the calculations presented in this paper, similar to prior studies of the SFH in NGC 1569 (McQuinn et al. 2010; Angeretti et al. 2005). The exact IMF choice does not affect the shape of the inferred SFH for the outer region of NGC 1569. This is because all observed stars have evolved off the main sequence, and have approximately the same mass. However, the IMF choice does affect the normalization of the SFH, since different IMF slopes predict different amounts of (unobserved) lower-mass stars for a given (observed) population of giants. The assumed binary fraction also affects the SFH normalization, because some single observed sources may have the mass of two stars. For the calculations in the paper the SFH shape was not found to depend sensitively on the assumed binary fraction, and all results reported herein assume a zero binary fraction. Our code has the option to assign different reddening to different stars in the basis functions. We did not use this feature for the outer region of NGC 1569. Our $H\alpha$ image showed very little emission there, so that differential reddening is not expected to be an issue.

REFERENCES

- Aloisi, A., Clementini, G., Tosi, M., Annibali, F., Contreras, R., Fiorentino, G., Mack, J., Marconi, M., Musella, I., Saha, A., Sirianni, M., & van der Marel, R. P. 2007, ApJ,

667, L151

- Aloisi, A., van der Marel, R. P., Mack, J., Leitherer, C., Sirianni, M., & Tosi, M. 2005, *ApJ*, 631, L45
- Anders, E. & Grevesse, N. 1989, *Geochim. Cosmochim. Acta*, 53, 197
- Anders, P., de Grijs, R., Fritze-v. Alvensleben, U., & Bissantz, N. 2004, *MNRAS*, 347, 17
- Angeretti, L., Tosi, M., Greggio, L., Sabbi, E., Aloisi, A., & Leitherer, C. 2005, *AJ*, 129, 2203
- Asplund, M., Grevesse, N., Sauval, A. J., & Scott, P. 2009, *ARA&A*, 47, 481
- Barker, M. K., Sarajedini, A., & Harris, J. 2004, *ApJ*, 606, 869
- Bekki, K., Couch, W. J., Beasley, M. A., Forbes, D. A., Chiba, M., & Da Costa, G. S. 2004, *ApJ*, 610, L93
- Bertelli, G., Bressan, A., Chiosi, C., Fagotto, F., & Nasi, E. 1994, *A&AS*, 106, 275
- Boyer, M. L., Skillman, E. D., van Loon, J. T., Gehrz, R. D., & Woodward, C. E. 2009, *ApJ*, 697, 1993
- Burstein, D. & Heiles, C. 1982, *AJ*, 87, 1165
- Caffau, E., Ludwig, H.-G., Steffen, M., Freytag, B., & Bonifacio, P. 2011, *Sol. Phys.*, 268, 255
- Cardelli, J. A., Clayton, G. C., & Mathis, J. S. 1989, *ApJ*, 345, 245
- Cioni, M., van der Marel, R. P., Loup, C., & Habing, H. J. 2000, *A&A*, 359, 601
- Cretton, N., de Zeeuw, P. T., van der Marel, R. P., & Rix, H. 1999, *ApJS*, 124, 383
- de Marchi, G., Clampin, M., Greggio, L., Leitherer, C., Nota, A., & Tosi, M. 1997, *ApJ*, 479, L27
- della Ceca, R., Griffiths, R. E., Heckman, T. M., & MacKenty, J. W. 1996, *ApJ*, 469, 662
- Devost, D., Roy, J.-R., & Drissen, L. 1997, *ApJ*, 482, 765
- Dolphin, A. E. 2002, *MNRAS*, 332, 91
- Fagotto, F., Bressan, A., Bertelli, G., & Chiosi, C. 1994a, *A&AS*, 104, 365

- . 1994b, *A&AS*, 105, 29
- Font, A. S., Johnston, K. V., Bullock, J. S., & Robertson, B. E. 2006, *ApJ*, 638, 585
- Fruchter, A., Sosey, M., Hack, W., Dressel, L., Koekemoer, A. M., Mack, J., Mutchler, M., & Pirzkal, N. 2009, “The MultiDrizzle Handbook”, version 3.0, (Baltimore, STScI)
- Gilbert, A. M. & Graham, J. R. 2002, in *IAU Symposium*, Vol. 207, *Extragalactic Star Clusters*, ed. D. P. Geisler, E. K. Grebel, & D. Minniti, 471
- Girardi, L., Bertelli, G., Bressan, A., Chiosi, C., Groenewegen, M. A. T., Marigo, P., Salasnich, B., & Weiss, A. 2002, *A&A*, 391, 195
- Girardi, L. & Salaris, M. 2001, *MNRAS*, 323, 109
- Girardi, L., Williams, B. F., Gilbert, K. M., Rosenfield, P., Dalcanton, J. J., Marigo, P., Boyer, M. L., Dolphin, A., Weisz, D. R., Melbourne, J., Olsen, K. A. G., Seth, A. C., & Skillman, E. 2010, *ApJ*, 724, 1030
- Greggio, L., Tosi, M., Clampin, M., de Marchi, G., Leitherer, C., Nota, A., & Sirianni, M. 1998, *ApJ*, 504, 725
- Greve, A., Becker, R., Johansson, L. E. B., & McKeith, C. D. 1996, *A&A*, 312, 391
- Grocholski, A. J., Aloisi, A., van der Marel, R. P., Mack, J., Annibali, F., Angeretti, L., Greggio, L., Held, E. V., Romano, D., Sirianni, M., & Tosi, M. 2008, *ApJ*, 686, L79
- Grocholski, A. J. & Sarajedini, A. 2002, *AJ*, 123, 1603
- Harris, J. & Zaritsky, D. 2001, *ApJS*, 136, 25
- Heckman, T. M., Dahlem, M., Lehnert, M. D., Fabbiano, G., Gilmore, D., & Waller, W. H. 1995, *ApJ*, 448, 98
- Hopkins, A. M. & Beacom, J. F. 2006, *ApJ*, 651, 142
- Hunter, D. A., Hawley, W. N., & Gallagher, III, J. S. 1993, *AJ*, 106, 1797
- Hunter, D. A., O’Connell, R. W., Gallagher, J. S., & Smecker-Hane, T. A. 2000, *AJ*, 120, 2383
- Israel, F. P. 1988, *A&A*, 194, 24
- Israel, F. P. & van Driel, W. 1990, *A&A*, 236, 323

- Ivezić, Ž., Sesar, B., Jurić, M., Bond, N., Dalcanton, J., Rockosi, C. M., Yanny, B., Newberg, H. J., Beers, T. C., Allende Prieto, C., Wilhelm, R., Lee, Y. S., Sivarani, T., Norris, J. E., Bailer-Jones, C. A. L., Re Fiorentin, P., Schlegel, D., Uomoto, A., Lupton, R. H., Knapp, G. R., Gunn, J. E., Covey, K. R., Smith, J. A., Miknaitis, G., Doi, M., Tanaka, M., Fukugita, M., Kent, S., Finkbeiner, D., Munn, J. A., Pier, J. R., Quinn, T., Hawley, S., Anderson, S., Kiuchi, F., Chen, A., Bushong, J., Sohi, H., Haggard, D., Kimball, A., Barentine, J., Brewington, H., Harvanek, M., Kleinman, S., Krzesinski, J., Long, D., Nitta, A., Snedden, S., Lee, B., Harris, H., Brinkmann, J., Schneider, D. P., & York, D. G. 2008, *ApJ*, 684, 287
- Izotov, Y. I. & Thuan, T. X. 1999, *ApJ*, 511, 639
- Jackson, M. C., Hunter, D., Oh, S., & LITTLE THINGS Team. 2011, in *Bulletin of the American Astronomical Society*, Vol. 43, American Astronomical Society Meeting Abstracts #217, 328.03
- Karachentsev, I. D. 2005, *AJ*, 129, 178
- Karachentsev, I. D., Dolphin, A., Tully, R. B., Sharina, M., Makarova, L., Makarov, D., Karachentseva, V., Sakai, S., & Shaya, E. J. 2006, *AJ*, 131, 1361
- Larsen, S. S., Origlia, L., Brodie, J., & Gallagher, J. S. 2008, *MNRAS*, 383, 263
- Lawson, C. L. & Hanson, R. J. 1974, *Solving least squares problems*, ed. Lawson, C. L. & Hanson, R. J.
- Marigo, P., Girardi, L., Bressan, A., Groenewegen, M. A. T., Silva, L., & Granato, G. L. 2008, *A&A*, 482, 883
- Marín-Franch, A., Aparicio, A., Piotto, G., Rosenberg, A., Chaboyer, B., Sarajedini, A., Siegel, M., Anderson, J., Bedin, L. R., Dotter, A., Hempel, M., King, I., Majewski, S., Milone, A. P., Paust, N., & Reid, I. N. 2009, *ApJ*, 694, 1498
- Martin, C. L., Kobulnicky, H. A., & Heckman, T. M. 2002, *ApJ*, 574, 663
- McQuinn, K. B. W., Skillman, E. D., Cannon, J. M., Dalcanton, J., Dolphin, A., Hidalgo-Rodríguez, S., Holtzman, J., Stark, D., Weisz, D., & Williams, B. 2010, *ApJ*, 721, 297
- Mühle, S., Klein, U., Wilcots, E. M., & Hüttemeister, S. 2005, *AJ*, 130, 524
- Origlia, L., Leitherer, C., Aloisi, A., Greggio, L., & Tosi, M. 2001, *AJ*, 122, 815

- Press, W. H., Teukolsky, S. A., Vetterling, W. T., & Flannery, B. P. 1992, Numerical recipes in FORTRAN. The art of scientific computing, ed. Press, W. H., Teukolsky, S. A., Vetterling, W. T., & Flannery, B. P.
- Rejkuba, M., Greggio, L., Harris, W. E., Harris, G. L. H., & Peng, E. W. 2005, *ApJ*, 631, 262
- Rejkuba, M., Harris, W. E., Greggio, L., & Harris, G. L. H. 2011, *A&A*, 526, A123
- Relaño, M., Lisenfeld, U., Vilchez, J. M., & Battaner, E. 2006, *A&A*, 452, 413
- Riess, A. & Mack, J. 2004, Time Dependence of ACS WFC CTE Corrections for Photometry and Future Predictions, Tech. rep.
- Robin, A. C., Reylé, C., Derrière, S., & Picaud, S. 2003, *A&A*, 409, 523
- Ryś, A., Grocholski, A. J., van der Marel, R. P., Aloisi, A., & Annibali, F. 2011, *A&A*, 530, A23
- Saha, A., Claver, J., & Hoessel, J. G. 2002, *AJ*, 124, 839
- Salpeter, E. E. 1955, *ApJ*, 121, 161
- Schlegel, D. J., Finkbeiner, D. P., & Davis, M. 1998, *ApJ*, 500, 525
- Schulte-Ladbeck, R. E., Hopp, U., Greggio, L., Crone, M. M., & Drozdovsky, I. O. 2001, *AJ*, 121, 3007
- Sirianni, M., Jee, M. J., Benítez, N., Blakeslee, J. P., Martel, A. R., Meurer, G., Clampin, M., De Marchi, G., Ford, H. C., Gilliland, R., Hartig, G. F., Illingworth, G. D., Mack, J., & McCann, W. J. 2005, *PASP*, 117, 1049
- Skillman, E. D. & Gallart, C. 2002, in *Astronomical Society of the Pacific Conference Series*, Vol. 274, *Observed HR Diagrams and Stellar Evolution*, ed. T. Lejeune & J. Fernandes, 535
- Stetson, P. B. 1987, *PASP*, 99, 191
- Stil, J. M. & Israel, F. P. 1998, *A&A*, 337, 64
- Sweigart, A. V., Greggio, L., & Renzini, A. 1990, *ApJ*, 364, 527
- Taylor, C. L., Hüttemeister, S., Klein, U., & Greve, A. 1999, *A&A*, 349, 424
- Tikhonov, N. A. & Galazutdinova, O. A. 2010, *Astronomy Letters*, 36, 167

- Tosi, M., Greggio, L., Marconi, G., & Focardi, P. 1991, *AJ*, 102, 951
- Vallenari, A. & Bomans, D. J. 1996, *A&A*, 313, 713
- van der Marel, R. P., Cretton, N., de Zeeuw, P. T., & Rix, H. 1998, *ApJ*, 493, 613
- Veilleux, S., Cecil, G., & Bland-Hawthorn, J. 2005, *ARA&A*, 43, 769
- Young, J. S., Gallagher, J. S., & Hunter, D. A. 1984, *ApJ*, 276, 476
- Zoccali, M. & Piotto, G. 2000, *A&A*, 358, 943



Fig. 1.— ACS/WFC 3-color image of NGC 1569, where the H α -, *I*- and *V*-bands have been colored red, orange, and blue, respectively. (The faint ellipse near the center of the field is the ghost image of a bright star).

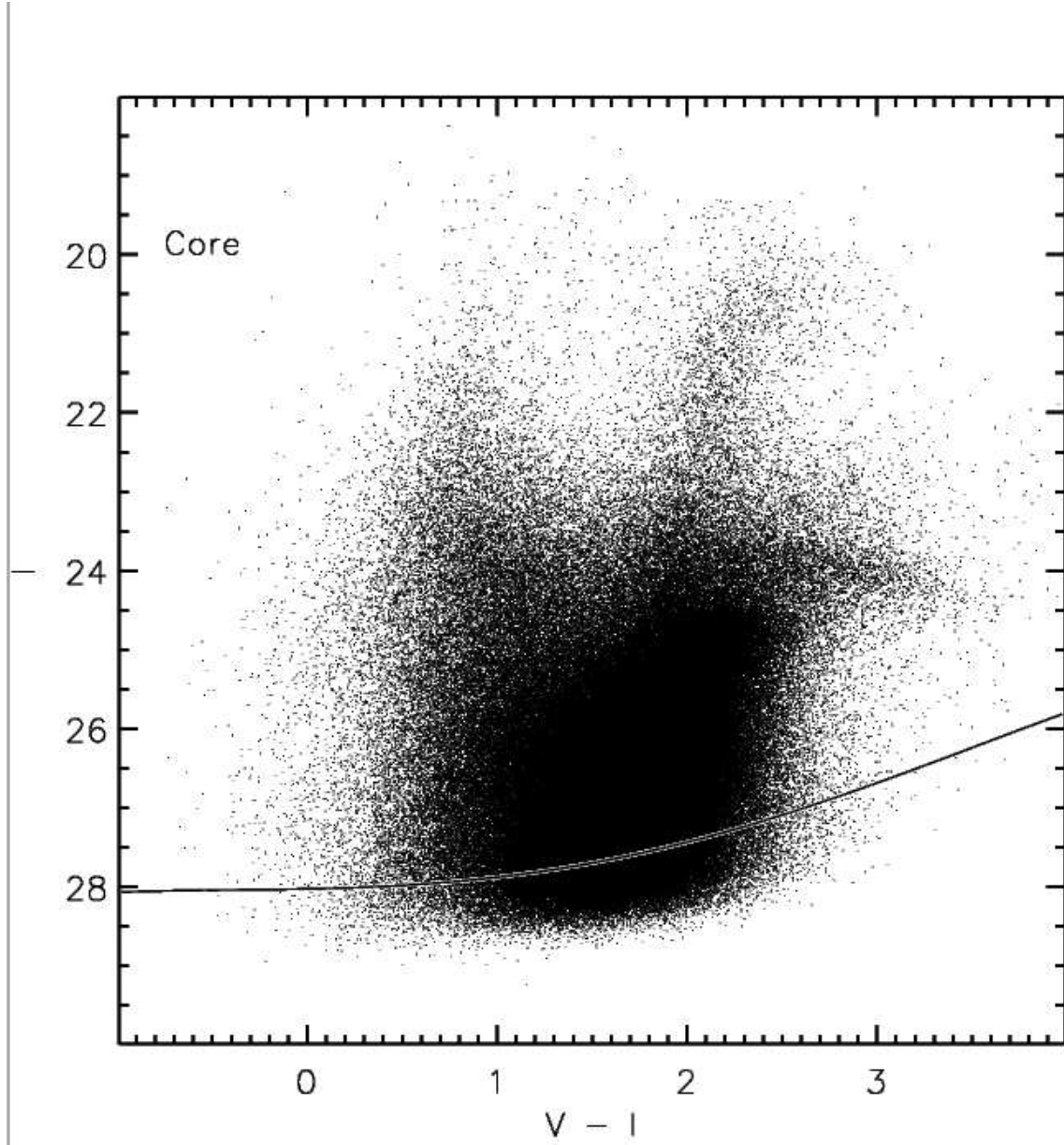


Fig. 2.— CMD composed of all stars in the core of NGC 1569 (bottom half of Fig. 1). Features resulting from young, massive, main sequence and evolved stars dominate the CMD (see §3 for details). The 20% completeness limit is shown as the solid line. The remainder of this paper focuses solely on the outer region of NGC 1569.

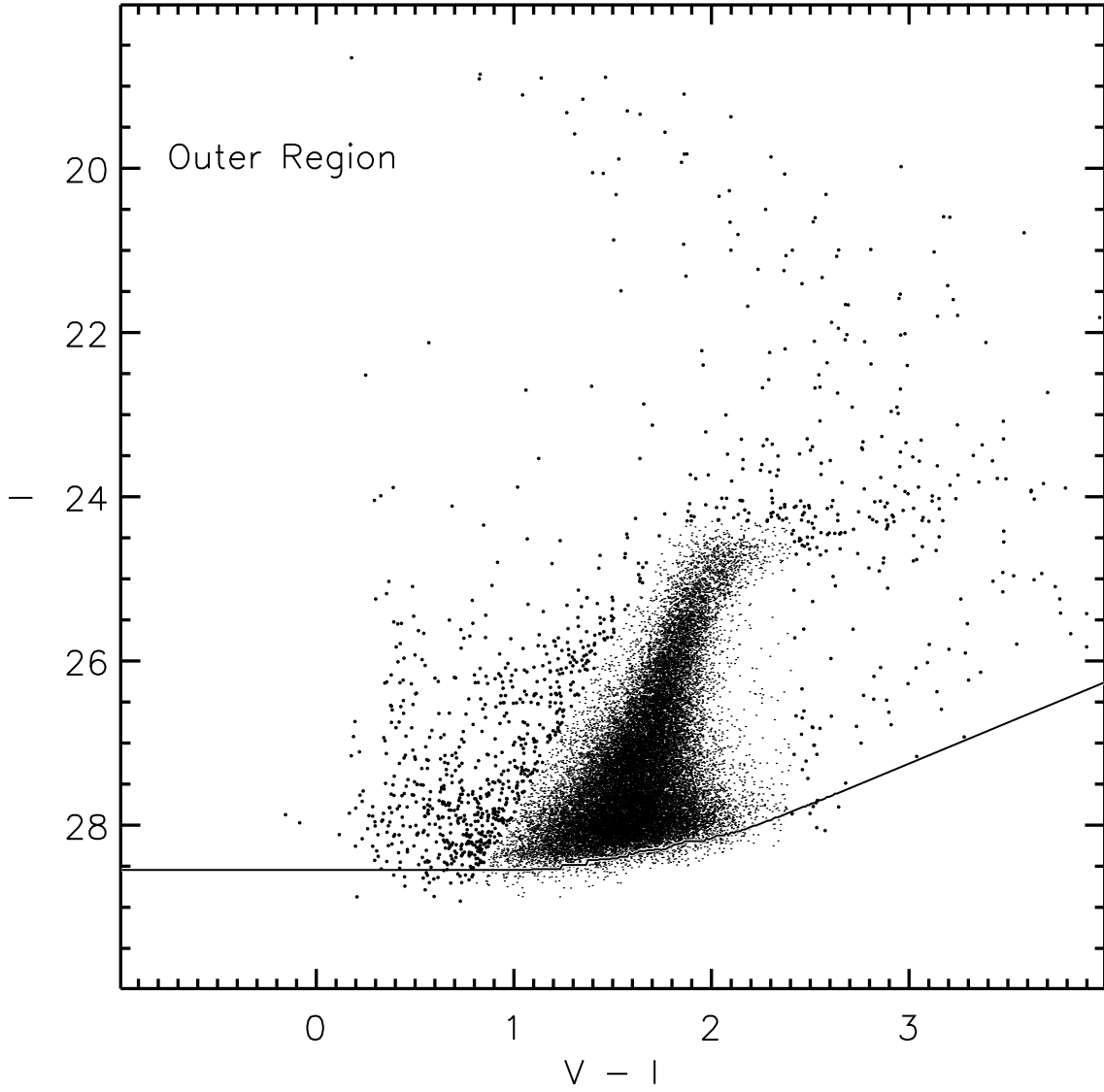


Fig. 3.— CMD of all stars in NGC 1569’s outer region (top half of Fig. 1). Unlike the core CMD, only the old stars on the RGB are readily visible in the outer region, illustrating that the recent star formation in NGC 1569 is concentrated in the core. For visibility, we have increased the size of the points for stars that are off of the RGB. As in the previous figure, the solid line represents the 20% completeness limit.

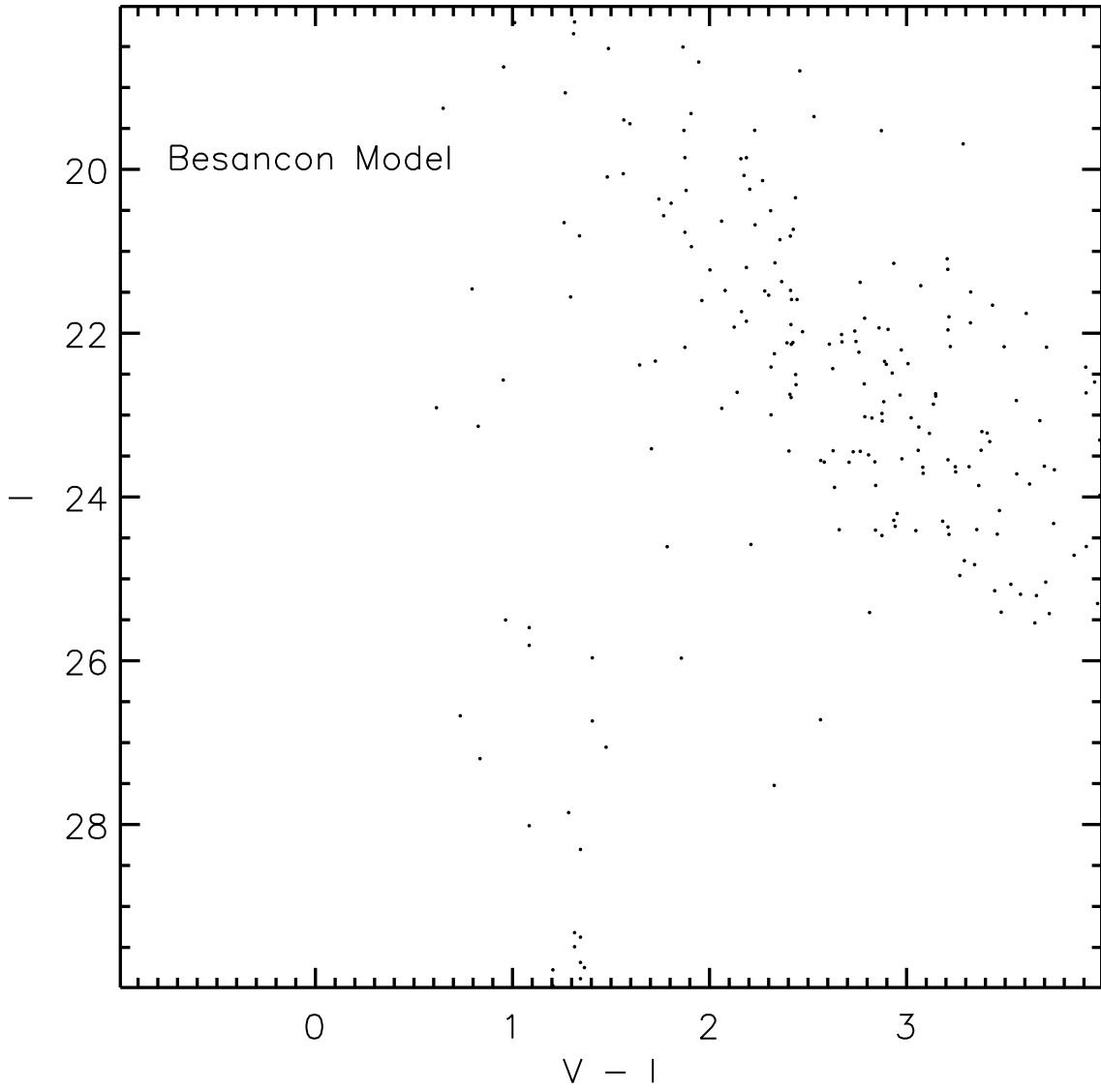


Fig. 4.— Besançon model of the expected MW foreground contamination in the direction of NGC 1569 (Robin et al. 2003), for a field size equal to that of the outer region (i.e., half of the total HST/ACS field).

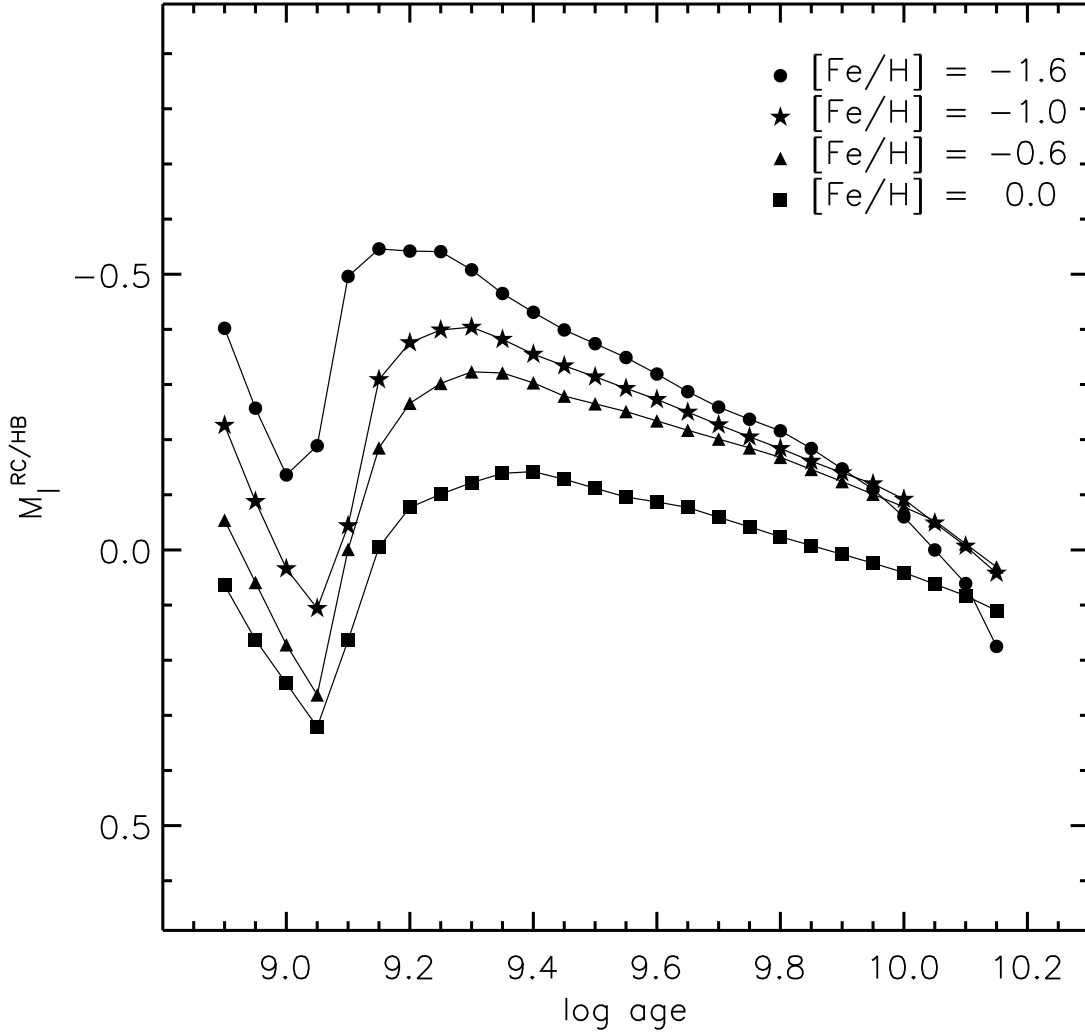


Fig. 5.— Absolute I -band magnitude of the RC/HB feature plotted as a function of age for a range of metallicities. For Figs. 5-7 we have used the theoretical values from the Padova isochrones.

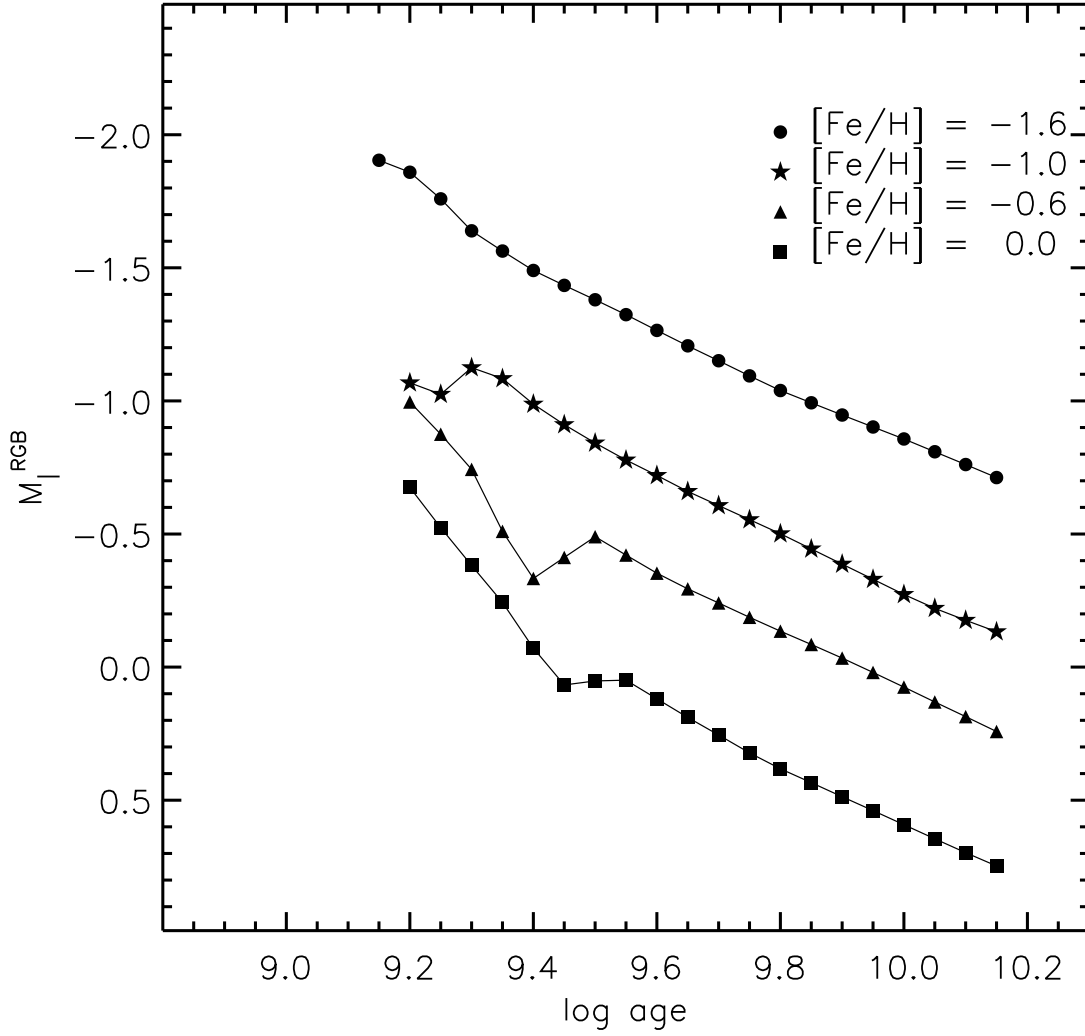


Fig. 6.— Absolute *I*-band magnitude of the RGB bump plotted as a function of age for a range of metallicities.

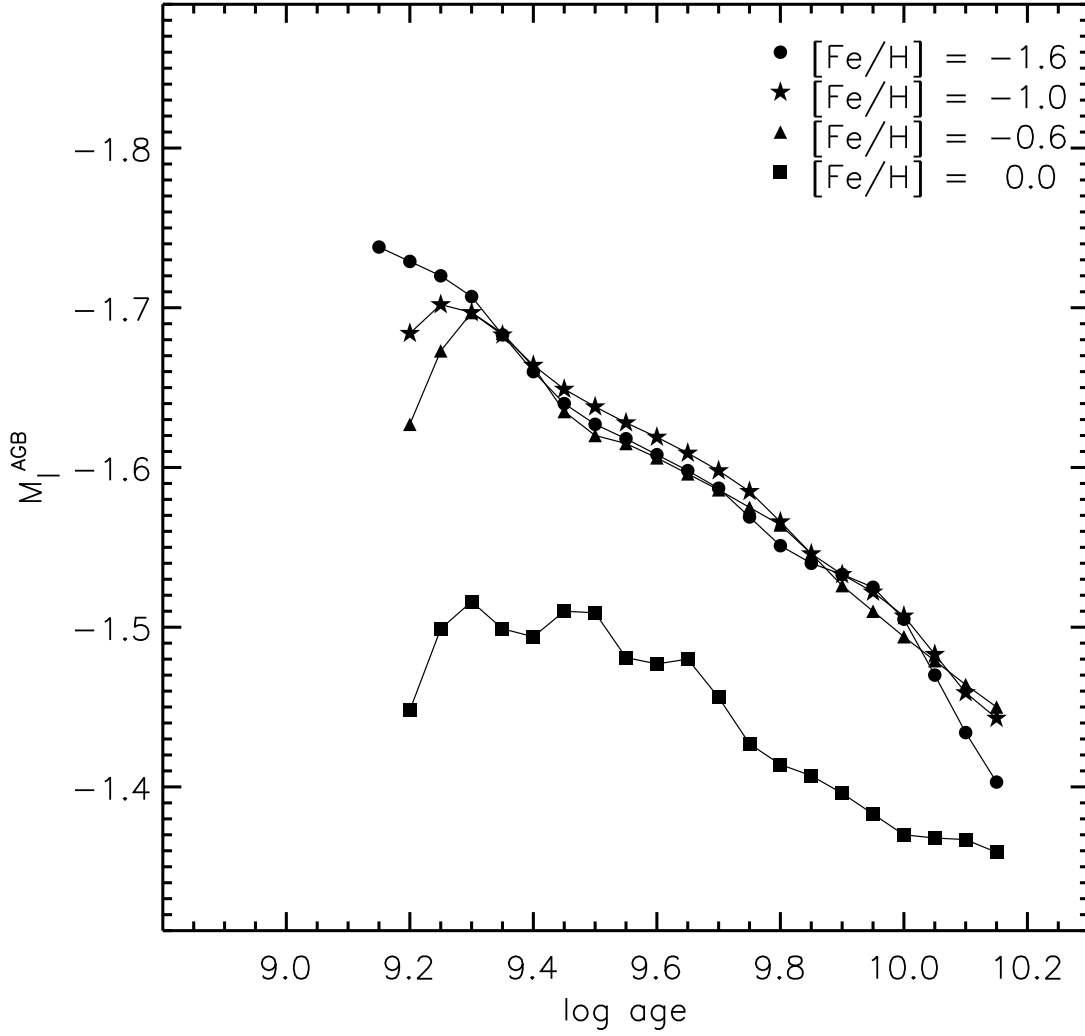


Fig. 7.— Absolute I -band magnitude of the AGB bump plotted as a function of age for a range of metallicities.

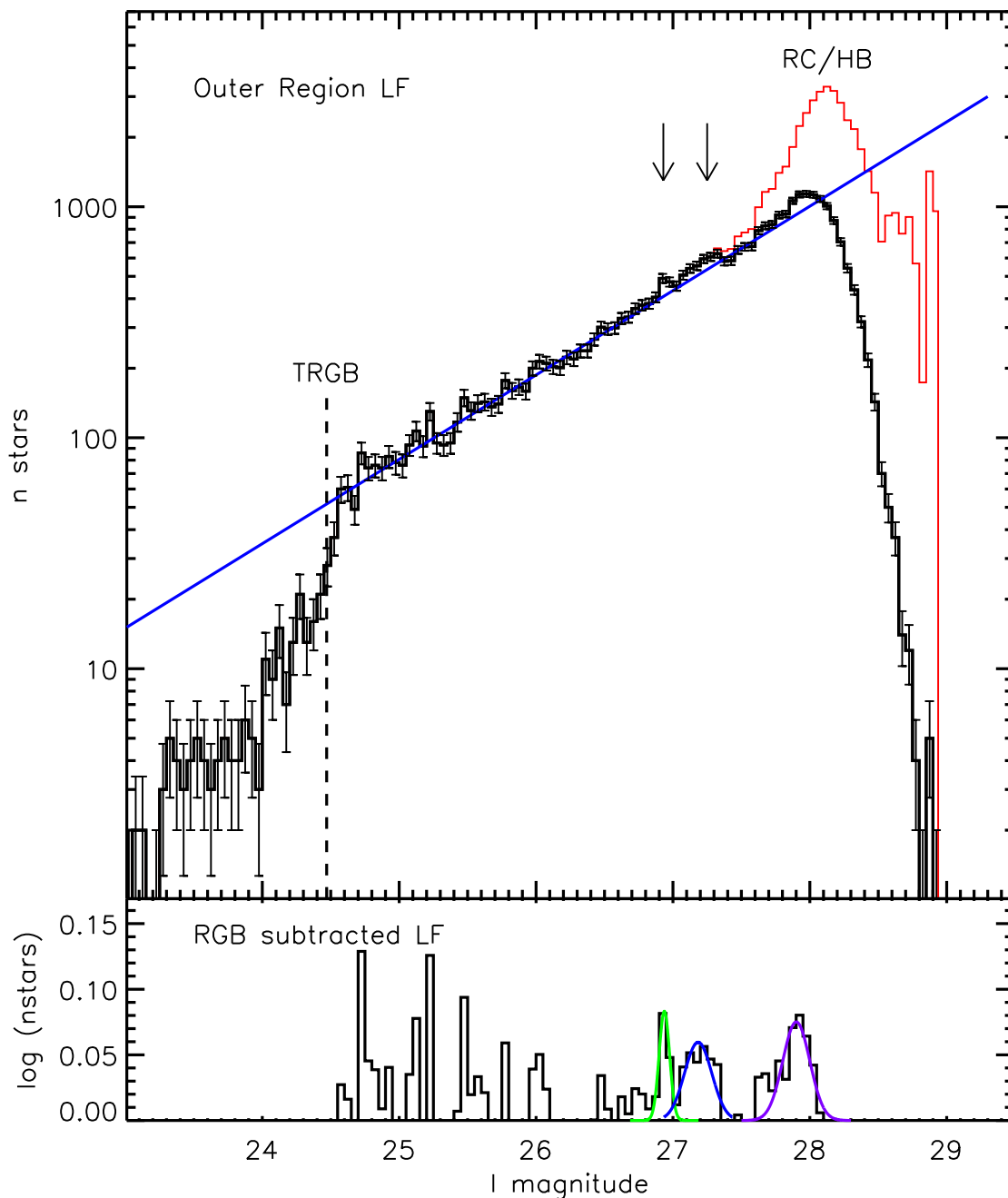


Fig. 8.— Observed (black line) and completeness corrected (thin red line) LFs of NGC 1569’s outer region. Brighter than $I \sim 27.3$, our photometry of NGC 1569’s outer region is $\sim 100\%$ complete. At $I = 28.4$ the completeness is only 20%, and the completeness correction is not very reliable beyond this magnitude. The vertical dashed line marks the position of the TRGB and the solid (blue) line follows the slope of the RGB. Three features of interest, the RC/HB (labeled) and the possible AGB bump and RGB bump features (arrows) are seen to extend above the expected RGB slope. Error bars overplotted on the observed LF show the Poisson noise in each magnitude bin and suggest that the possible AGB bump and RGB bump features may be real. The bottom panel shows the RGB slope-subtracted LF, with gaussian fits to the three features overplotted.

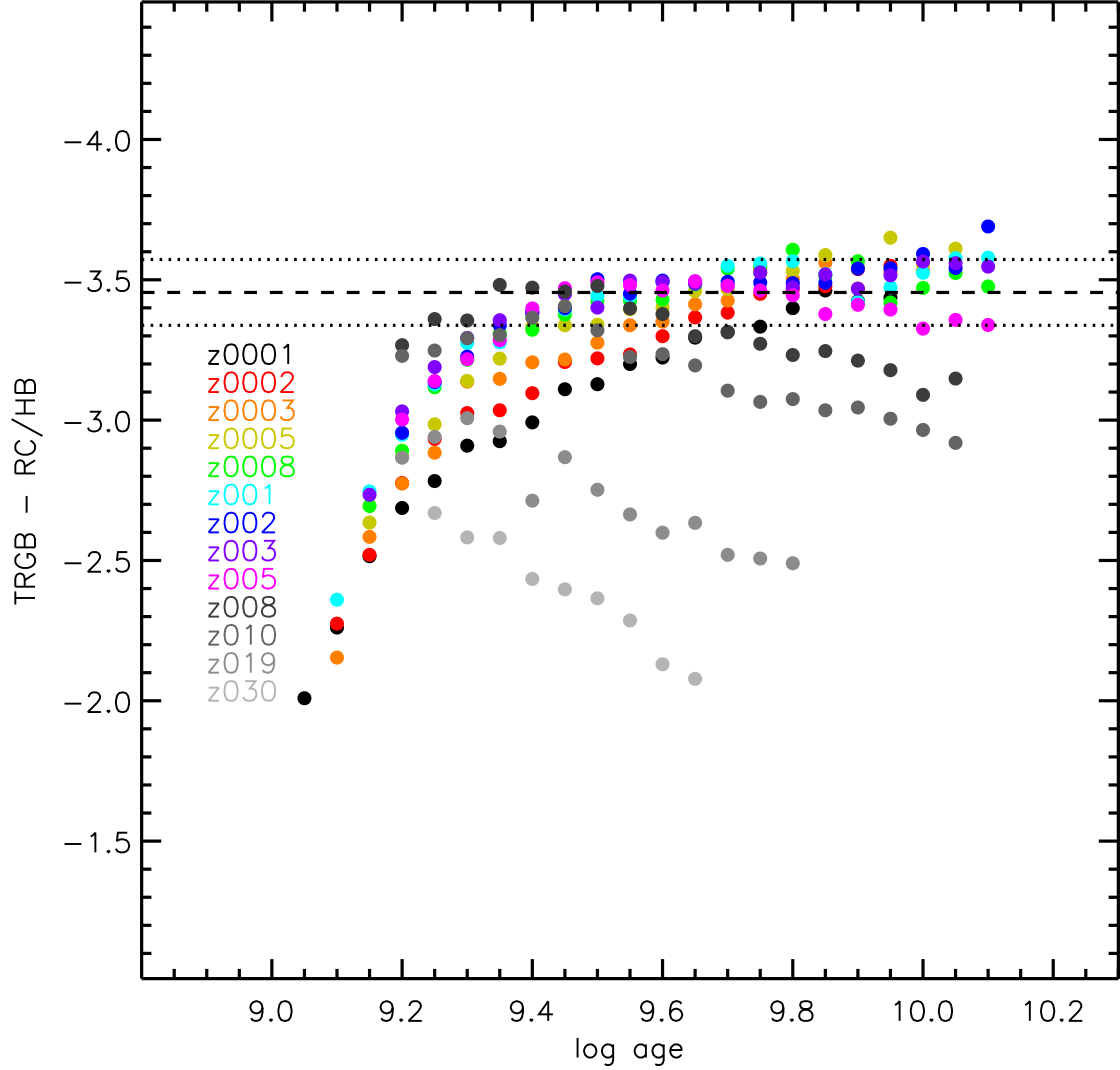


Fig. 9.— Difference in I -band magnitude of the TRGB and RC/HB as a function of age. Theoretical values for a range of metallicities (shown as symbols of different colors) were calculated by creating a synthetic CMD for each isochrone using our SFH code, which takes into account errors and incompleteness, and measuring the brightness of the features in the same way as for NGC 1569. The dashed line is our measured TRGB-RC/HB value for stars in NGC 1569’s outer region while the dotted lines mark the 3σ error in our measurement. Only those isochrones with TRGB-RC/HB values within 3σ of our measured value are considered as possible matches to NGC 1569.

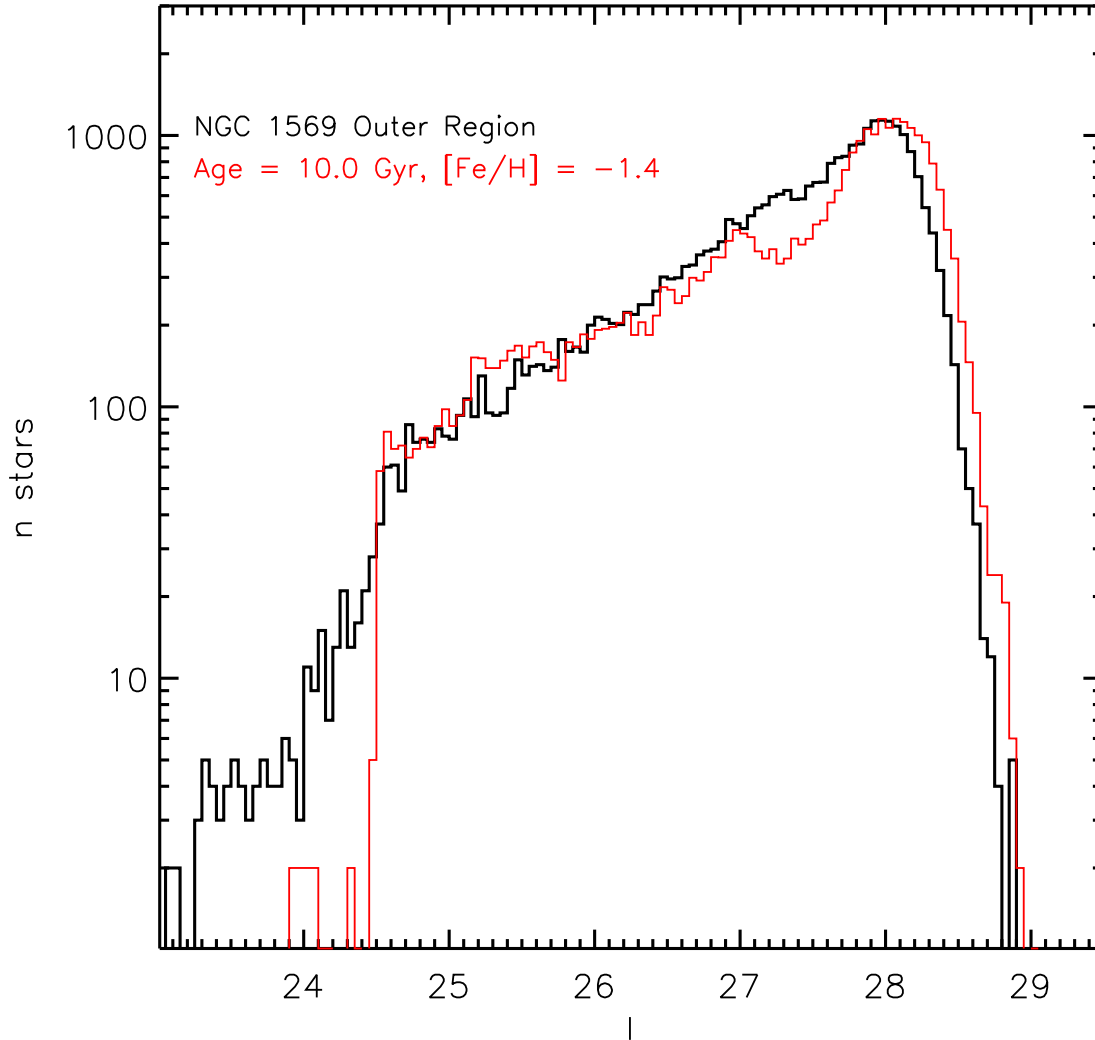


Fig. 10.— Theoretical SSP LF (thin red line) compared to NGC 1569’s outer region LF (black line). The synthetic LF shown, with an age of 10 Gyr and $[\text{Fe}/\text{H}] = -1.4$, provides the best simultaneous match to the positions of the AGB bump and RC/HB relative to the TRGB, to within our measurement errors. At this age and metallicity, the RGB bump is faint enough that it blends in with the RC/HB. While this synthetic population provides the best match, its LF features are much more pronounced and its LF slope flatter than what we observe. This difference suggests that NGC 1569’s outer region is not an SSP. Instead, it must have undergone many epochs of star formation, which served to both smooth the LF features and make it steeper.

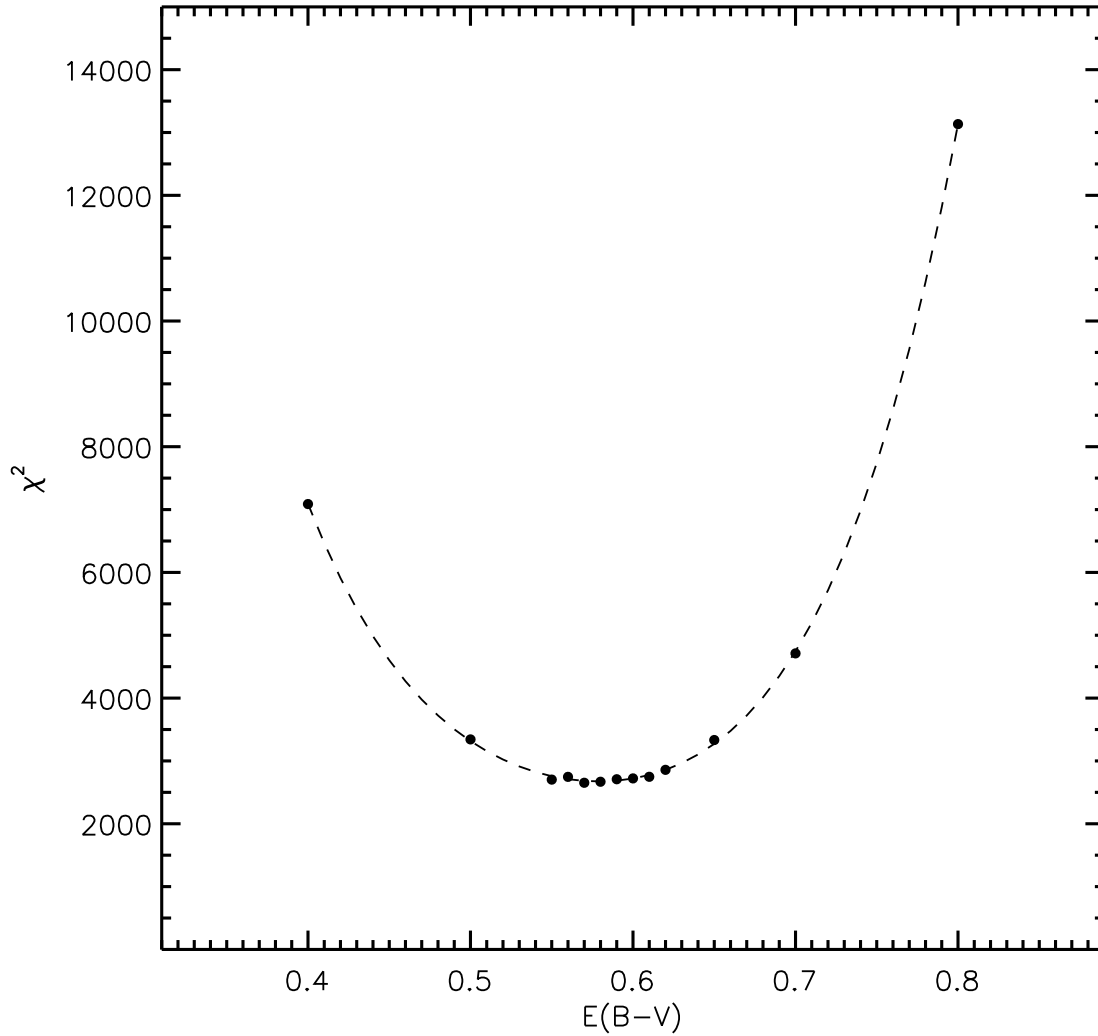


Fig. 11.— χ^2 of our SFH model fits to the CMD as a function of reddening. The χ^2 values vary smoothly with $E(B - V)$ and are well fit with a 4th order polynomial (dashed curve). The fit has a minimum at $E(B - V) = 0.58$. At this best-fit reddening, the galaxy distance implied by the TRGB magnitude is 3.06 Mpc.

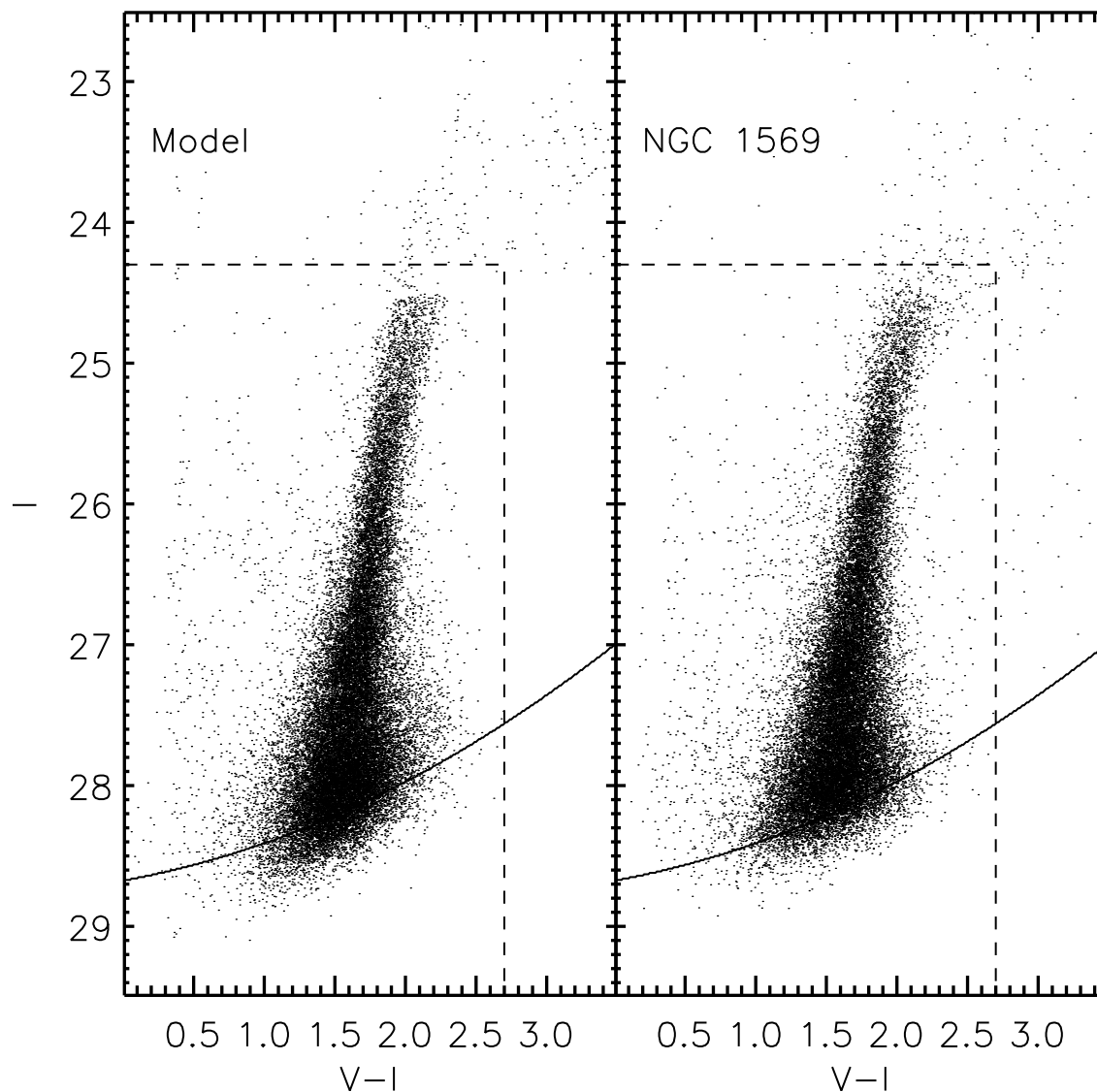


Fig. 12.— Comparison of the observed CMD (right) to a synthetic CMD realization (left) from the best-fit SFH. The areas below the solid line and above and to the right of the dashed box were excluded from the fit. At the faint magnitudes the completeness is too low ($< 20\%$) to yield an accurate fit. At the bright magnitudes there are foreground stars (see Fig. 4) and TP-AGB stars, a complex state of stellar evolution that has historically been difficult to model. The model matches the data well in the RGB region that was fit.

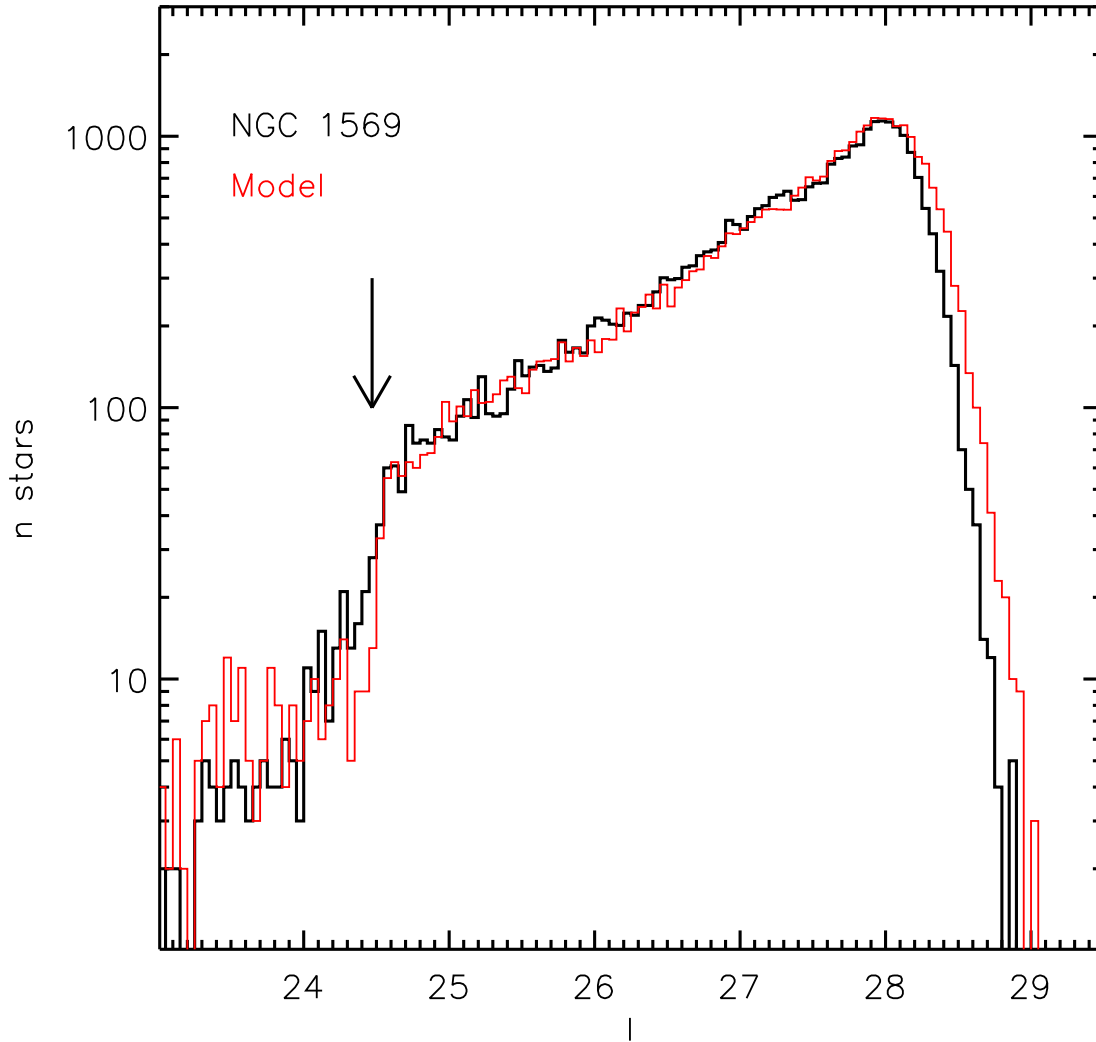


Fig. 13.— Luminosity function of NGC 1569 (black line) compared to the model LF for the best-fit SFH (thin red line). The TRGB is marked with the arrow. The isochrones slightly overpredict the number of TP-AGB stars brighter than $I \sim 24$. Below the TRGB, the model provides excellent agreement with the data. Discrepancies at $I \gtrsim 28$ are due to the limitations of artificial star test corrections when the incompleteness gets very low.

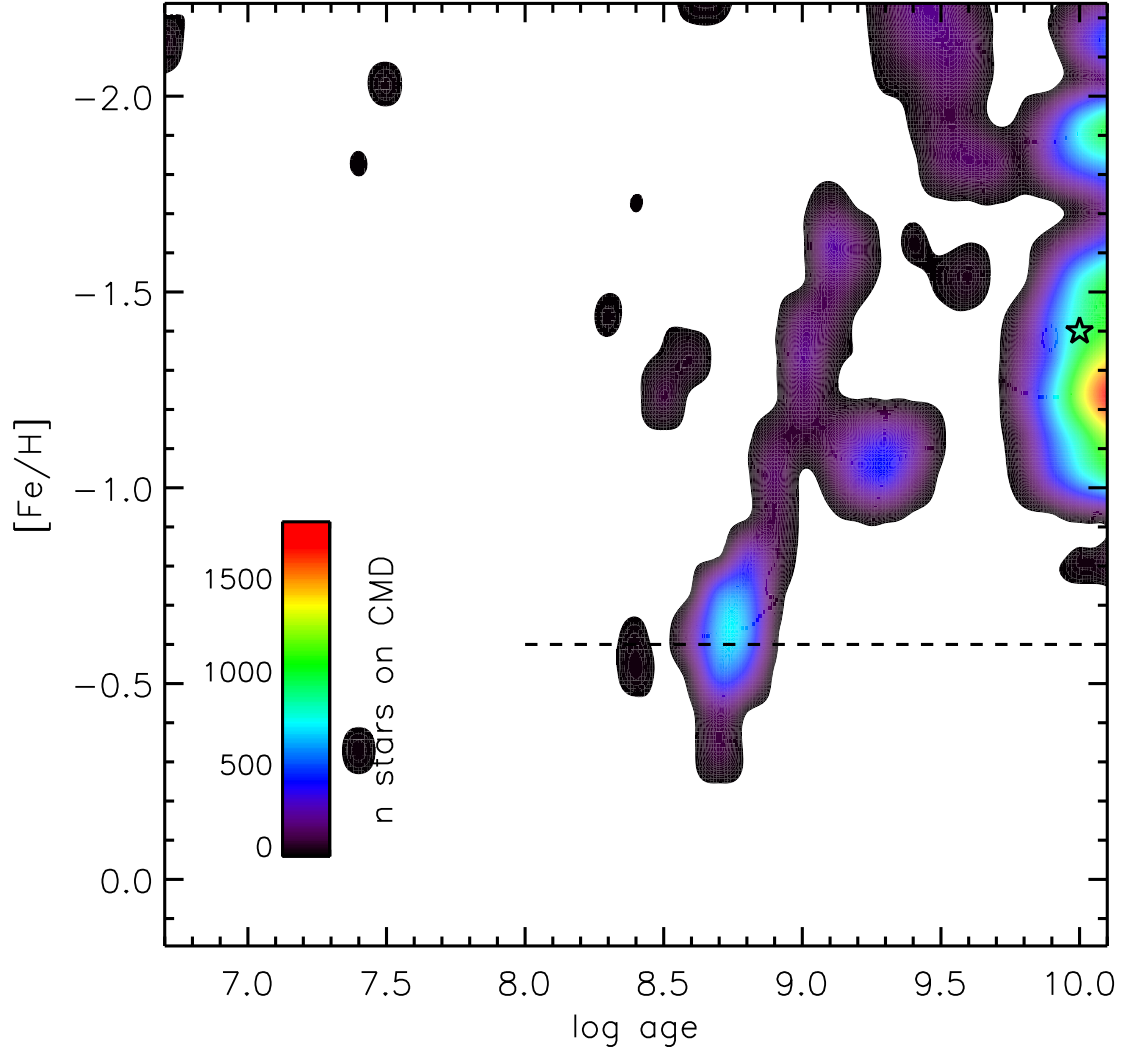


Fig. 14.— Contour plot of the SFH of the NGC 1569 outer region, interpolated onto a grid with a step size of 0.01 in both $\log(\text{age})$ and $[Fe/H]$. The color coding indicates the predicted number of stars on the parts of the CMD that are not masked in Fig. 12. The open star marks the position of the best-fitting SSP model as derived in §4.2. The dashed line indicates the abundance of the gas in NGC 1569. The properties and interpretation of this SFH are discussed in §5.

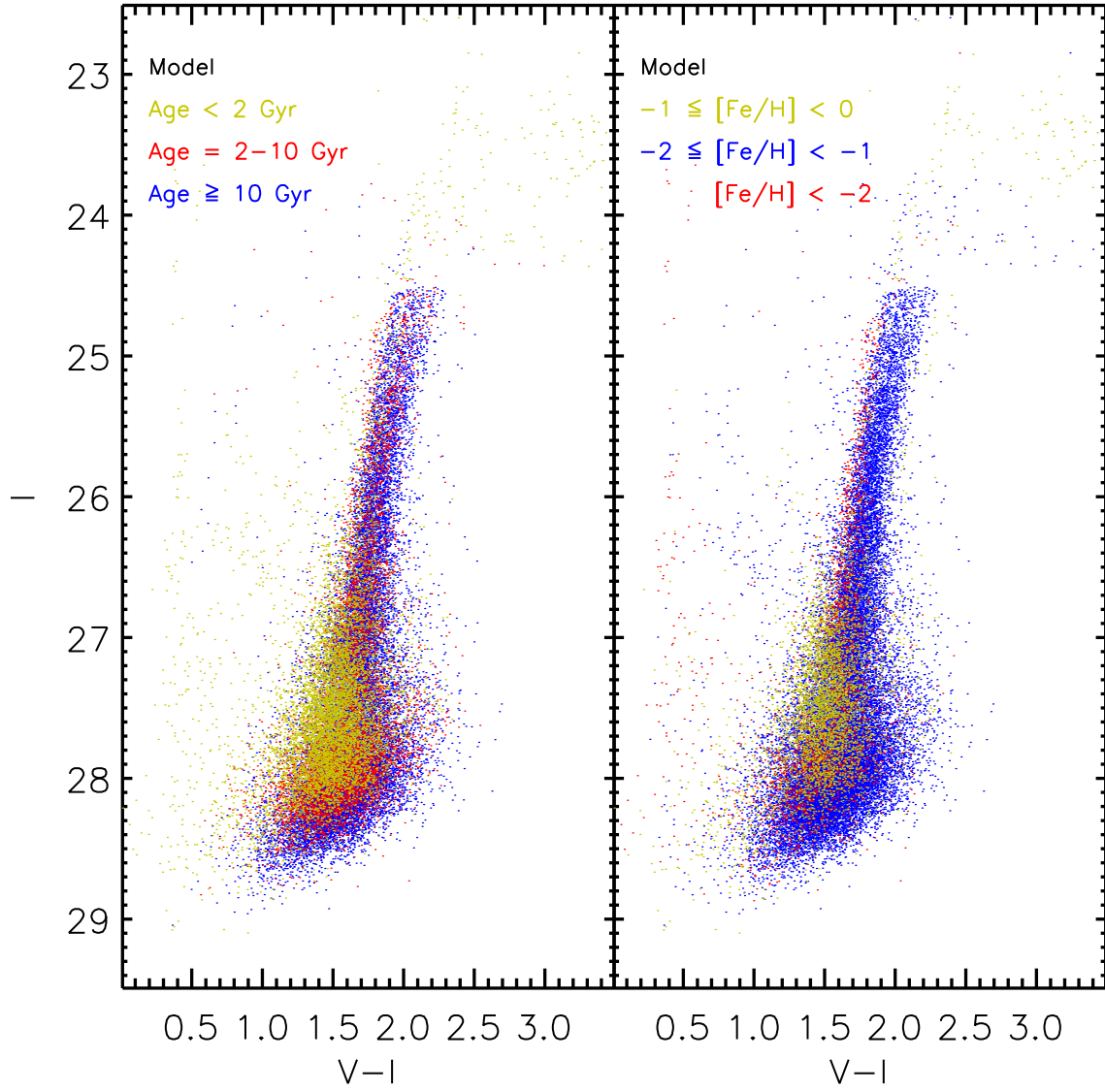


Fig. 15.— A synthetic CMD realization from the best-fit SFH. Different colors indicate a break-down into separate age (*left*) and metallicity (*right*) components. Stars in yellow correspond to a young and metal-rich component that steepens the RGB LF at the faint end, in accordance with the observations.

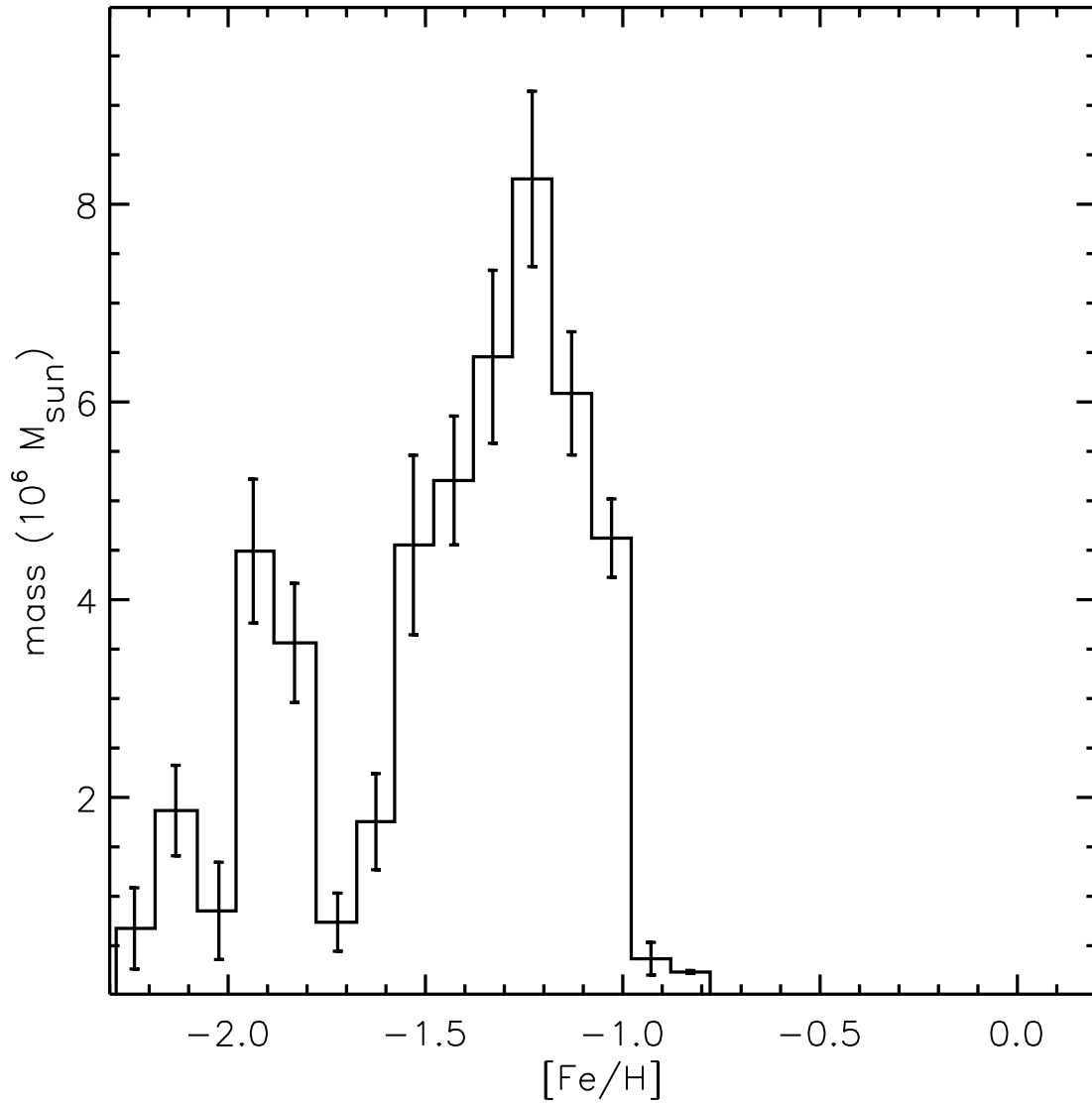


Fig. 16.— Stellar mass in the best-fit SFH vs. $[\text{Fe}/\text{H}]$, for those stars with $\log(\text{age}) \geq 9.7$. Error bars were calculated using bootstrapping as described in Appendix A. The old stars shown in this figure show a significant spread in metallicity, ranging between $[\text{Fe}/\text{H}] = -1$ and -2 .

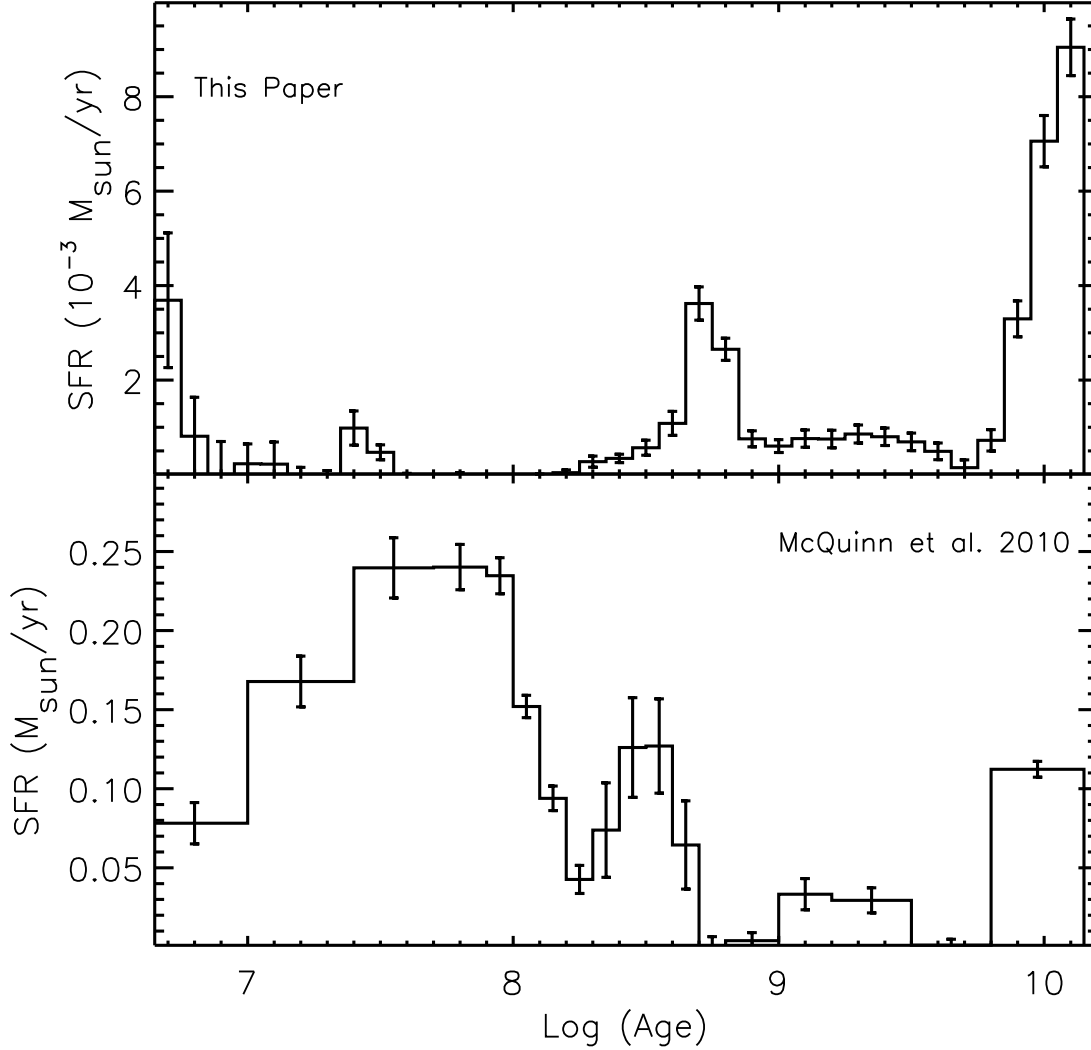


Fig. 17.— SFR as function of $\log(\text{age})$, integrated over all metallicities. (*top*) NGC 1569 outer region, as derived in the present paper. (*bottom*) NGC 1569 total, heavily dominated by the core, from McQuinn et al. (2010). The core shows much elevated star formation at young ages. But for the more ancient populations, our studies are in good overall agreement: most of the old stars formed ~ 10 Gyr ago; a low but significant amount of star formation persisted between 1 and 10 Gyr ago; and there was a SF peak/burst at $\sim 0.3\text{--}0.7$ Gyr ago.